8-27-2012

Influence of implementing straps on pulsed relativistic magnetron operation

David R. Galbreath

David Galbreath
Candidate

Electrical and Computer Engineering
Department

This thesis is approved, and it is acceptable in quality and form for publication:

Approved by the Thesis Committee:

Dr. Edl Schamiloglu, Chairperson

Dr. Sarita Prasad

Dr. Mark Gilmore

INFLUENCE OF IMPLEMENTING STRAPS ON PULSED RELATIVISTIC MAGNETRON OPERATION

by

DAVID GALBREATH

B.S.E., ELECTRICAL ENGINEERING, ORAL ROBERTS UNIVERSITY, 1996-2002

THESIS

Submitted in Partial Fulfillment of the
Requirements for the Degree of

Master of Science in Electrical Engineering

The University of New Mexico
Albuquerque, New Mexico

July, 2012

ACKNOWLEDGEMENTS

I would like to thank Dr. Edl Schamiloglu, my advisor and thesis chair, for his support and patience and his willingness to work with me long distance.

To Sarita Prasad, thank you for the guidance, encouragement and quick responses to my numerous questions.

Most importantly, I thank my wife, Sheila, and children, Aidan, Evan and Mahima. Your understanding and willingness to deal with me when I was scrambling to finish my work is a true sign of your love.

INFLUENCE OF IMPLEMENTING STRAPS ON PULSED RELATIVISTIC MAGNETRON OPERATION

by

David Galbreath

B.S.E., Electrical Engineering, Oral Roberts University, 2002

M.S., Electrical Engineering, University of New Mexico, 2012

ABSTRACT

A simulation study on the effect of applying straps to an A6 relativistic magnetron was conducted to determine potential use in reducing mode competition. Several strap configurations were evaluated against the basic anode-endcap geometry of the A6 magnetron as well as the open anode geometry. The effect of cathode radius on the primary mode of oscillation was also investigated in an effort to determine whether the use of straps could reduce mode competition. Typically the magnetron oscillates in the π-mode at small cathode radii and 2π-mode at large radii.

In general, strapping appears to offer several advantages for use in the A6 magnetron. For conditions where the A6 performs well, replacing the anode endcaps with either a double strap or a single strap tied to each vane produced 10-15% greater output power with an increase in operating efficiency as well. For conditions where the A6 does not perform well, such as when employing a small radius cathode, the double strap reduced the mode competition observed in many cases.

TABLE OF CONTENTS

LIST OF FIGURES

LIST OF TABLES

CHAPTER 1 - INTRODUCTION

Multi-cavity magnetrons in general have been under development since at least 1937 in Russia and were used by various countries during World War II for early radars [1]. These magnetrons, in turn, were based on even earlier designs by Gerdien and Hull as far back as 1910 [2]. Since that time, multi-cavity magnetrons have developed in multiple directions, from use in microwave ovens to numerous radar applications and other industrial uses.

Conventional magnetrons, those operating with input voltages of less than 100 kV and input currents on the order of 100 A, have developed to the point that several operate at 90% efficiency [3]. One of the innovations used to improve that efficiency is the use of strapping, a method of electrically tying alternating vanes of the anode block together. This strapping has been shown to increase the operating efficiency of the conventional magnetron significantly while decreasing mode competition.

Relativistic magnetrons, on the other hand, can produce several hundred megawatts to a few gigawatts of output power (peak output during a short pulse) depending on the frequency used but are characterized by much lower efficiencies, typically on the order of 20-35% [3]. Various efforts have been made to improve this situation, but to-date the use of straps seems to have been largely neglected.

1.1 Relativistic Magnetrons

A relativistic magnetron operates similarly to a conventional magnetron such as those used in microwave ovens or other commercial and industrial applications. A brief description of the operation of a generic magnetron follows, based largely on descriptions

and explanations provided in [4-8]. This description is offered qualitatively; a more formal discussion follows in Chapter 2.

Electrons are emitted from the negatively charged cathode with an initial velocity that can vary significantly depending on the method and strength of emission. Devoid of any external fields, these electrons would travel in a straight line, generally directly toward the anode. However, magnetrons utilize both an electric field, oriented across the anode-cathode (A-K) gap, and a magnetic field, oriented axially down the length of the magnetron [5]. The magnetic field, either generated by permanent magnets in a typical oven magnetron or by energizing a powerful electromagnetic coil for high power applications, combined with the electric field, curves the electron trajectory. Figure 1.1, excerpted from Fig. 13.3 and 13.4 in [6], demonstrates these effects on an electron's path. Depending on the relative strengths of these two fields, any of several possible cyclical paths are possible, some of which are shown in Fig. 1.2, excerpted from Fig. 13.5 also in [6]. The magnetic and electric fields are oriented at right angles to each other, hence the classification of the magnetron as a crossed field device.

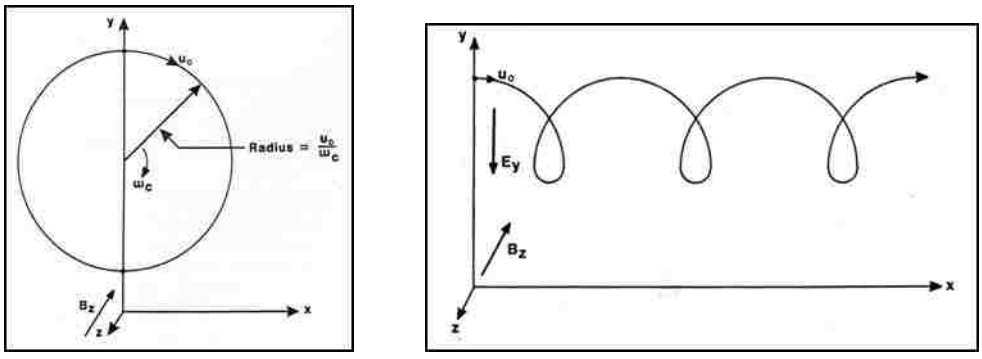

Figure 1.1. Electron orbit in a magnetic field in the absence of an electric field (left) and cycloidal electron trajectory in the presence of a y-directed electric field (right) [6].

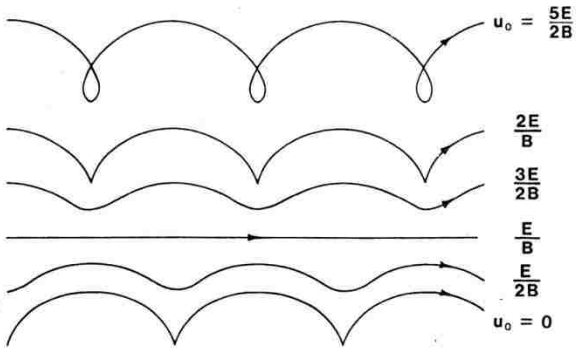

Figure 1.2. Electron trajectories for various initial velocities or electric field levels [6].

As the electrons orbit the cathode, they are forced closer together by the continuing emission of additional electrons from the cathode with the electric field pushing them back toward the cathode and the shearing acceleration imposed by the magnetic field. This causes the initial clustering of particles seen around the cathode in the early stages of operation.

As electrons are emitted from the cathode, there is a range of possible initial velocities; some of these velocities will match the phase velocities of resonant modes in the slow wave structure (SWS) of the anode. These electrons will interact with the RF fields, causing the field to grow in amplitude faster than fields for any non-resonant phase velocities. The electrons that are out of phase with the RF field take energy from the RF fields and are accelerated towards the cathode where they are either reabsorbed in the cathode or produce secondary electrons. The electrons that are in phase with the RF field are decelerated towards the anode where they lose their energy to the RF fields. This form of interaction of the electrons with the RF fields leads to spoke formation [8].

1.2 Mode Competition in Magnetrons

A primary limitation of magnetrons is the constant presence of competing modes. While the desired frequencies radiate the most efficiently, some of the input energy is

wasted on degenerate modes that do not resonate efficiently or are not effectively radiated through the extraction port. Due to the manner in which resonating frequencies are grown out of the general background noise, these degenerate modes cannot be completely eliminated.

Lemke *et al.* [9] theorized that one of the limiting factors in relativistic magnetron efficiency noted as space charge density increases is spoke expansion, in other words, increased charge density in the electron cloud pushing some electrons out of the desired orbit into less efficient orbits oscillating at a different frequency. This effect may also contribute to the continued resurgence of competing modes.

Regardless of the causes, these effects contribute to the comparatively low efficiency observed in relativistic magnetrons. The competing modes of greatest concern are typically close to the desired modes. Several methods have been employed in conventional magnetrons to reduce these effects.

The first method, which has been used with significant effect in relativistic magnetrons as well, is referred to as the rising sun geometry. This approach uses two different sizes for the alternate sets of vanes to force π-mode oscillations and increase the separation between the π-mode and the next lower resonant frequency. Essentially, the rising sun geometry can be considered as two resonator systems coupled together [7] with the π-mode being the common mode between the two resonator systems.

While the rising sun approach is effective, often yielding a higher efficiency than the A6 geometry, it also introduces another limiting problem involving the 0^{th}-spatial harmonic [9]. This harmonic is peculiar to the rising sun geometry and forces an upper limit to the efficiency of rising sun magnetrons.

1.3 Magnetron Strapping

Another solution to mode competition that has been used effectively in non-relativistic magnetrons is known as strapping and is the focus of this thesis. Strapping has been employed in conventional magnetrons since at least 1950 [10]. Conceptually, strapping is simply a matter of electrically connecting alternate vanes of the anode SWS to facilitate the growth of the desired π-mode while suppressing other less efficient modes.

Typically, two straps are used on each end of the SWS so that all of the vanes are tied into one of two sets. In a conventional magnetron, this arrangement encourages the development of the preferred π-mode oscillations by increasing the separation between the π-mode wavelength and other viable mode wavelengths. Effectively, the strap adds a capacitance for the π-mode and an inductance for other modes of oscillation, thereby altering the frequency of the preferred mode more significantly than the other modes [6].

A recognized limitation to the practical application of strapping to relativistic magnetrons is the strong potential for arcing in the vicinity of the straps [5]. However, this should only occur when the straps and the adjacent vane are at significantly different potentials, a condition which is minimized during 2π-mode operation. During π-mode operation this may still occur between the straps and the unstrapped vane; mode contamination will likely worsen this condition. This work does not propose to solve this problem but rather determine whether the potential benefits justify attempts at solving that problem.

1.4 Outline of Thesis

This thesis is developed as follows.

Chapter 2 discusses the basic characteristics of the magnetron, both conventional and relativistic, and discusses some of the principle limitations in their operation. Chapter 2 continues with a description of strapping and its effects on the conventional magnetron.

Chapter 3 details the simulations performed and discusses the rationale for some of the simulation choices presented. It continues with a description of the simulation results.

Chapter 4 addresses some questions that may arise from the literature based on non-relativistic magnetron strapping and details the conclusions drawn from the simulations. Finally, further avenues of research that might be pursued are discussed.

CHAPTER 2 - MAGNETRON OPERATION AND STRAPPING

In this chapter, the preceding discussion on magnetron operation and strapping will be expanded with a more rigorous discussion of the processes involved. The basic concepts behind magnetron operation are discussed first with strapping explained in detail next.

2.1 Theory of Magnetron Operation

Magnetrons typically feature a central cathode in a vacuum chamber, the outer walls of the chamber forming the anode. This anode is shaped to serve as a slow wave structure (SWS), which acts on the RF field in the chamber by slowing the angular phase velocity. A DC electric field is applied to the device radially between the cathode and the anode while a magnetic field is applied axially to the magnetron either through the use of permanent magnets or an electromagnetic coil. In general, both of these fields are considered to be constant during magnetron operation. Research has been performed incorporating variations in the magnetic field to contribute to magnetic priming of the magnetron both in conventional magnetrons [5, 11] and later expanded to relativistic magnetrons as well [12] but was not applied in this work.

Multiple factors affect the performance of a given magnetron, including the geometry of the magnetron, method of power extraction, input voltage and magnetic field, to name four of the most significant. While some attempts at numerical analysis of magnetrons have been attempted for various portions of the magnetron [13, 14] the effects of varying the physical geometry preclude ready analysis which has contributed significantly to the development of the numerous computer aided tools available for analysis of magnetron designs [15].

As electrons are emitted from the cathode, the magnetic field, oriented at right angles to the initial velocity, will cause their path to curve around the cathode and, depending on the field levels involved, may prevent them from reaching the anode completely. The DC electric field, aligned radially across the A-K gap, accelerates the electrons toward the cathode. There exists a cutoff point where the magnetic and electric fields are balanced such that the electrons just barely reach the anode; this is known as the Hull cutoff condition and is modified slightly from Equation 6.5 in [5] for a cylindrical geometry magnetron as

$$B_H = \frac{2b}{b^2 - a^2}\left(\frac{2m_o V}{|e|}\right)^{\frac{1}{2}}\left[1 + \frac{1}{2}\frac{|e|V}{m_0 c^2}\right]^{\frac{1}{2}} \tag{1}$$

where b is the inner radius of the vanes, a is the cathode radius, m_0 is the rest mass of the electron, $|e|$ is the electron charge and c is the speed of light. Considering b and a to be constant for a given magnetron design, it becomes clear that (1) provides a relation between the driving voltage and the minimum allowable magnetic field; below this value, the electrons simply follow the electric field lines and are absorbed in the anode block without contributing to the microwave energy.

A second guiding equation for magnetron operation provides an operating regime for the magnetic field by defining the field level where the electron's initial orbital velocity is matched with the electromagnetic wave's phase velocity (v_{ph}). This condition is known as the Buneman-Hartree resonance condition and is defined by Equation 6.4 again in [5] as

$$V_{BH} = B_0 \frac{(b^2 - a^2)}{2b} v_{ph} - \frac{m_0 c^2}{2|e|}\left\{1 - \left[1 - \left(\frac{v_{ph}}{c}\right)^2\right]^{1/2}\right\} \tag{2}$$

Again it is noted that the magnetic field and the electric field (voltage) are the only variables, the rest being constants or, in the case of v_{ph}, predetermined by the geometry of the SWS in the magnetron and mode in question.

Once the magnetic field exceeds this resonance condition for a given voltage, the magnetron approaches a cutoff condition where the emitted electrons no longer have sufficient initial velocity to overcome the magnetic field acceleration, prohibiting the electrons from approaching the anode and limiting their ability to contribute energy to the RF field.

The resonance condition becomes a key factor in effective operation of the magnetron as it is only when the electrons are orbiting at or near this resonance condition that they effectively yield energy to the RF oscillations.

As discussed in Chapter 1, as the electrons are emitted into the A-K gap, they encounter a force resulting from the crossed electric and magnetic fields leading them to orbit the cathode. The rate at which they will escape toward the anode depends on the density of the electron cloud and the Hull cutoff relation described in (1).

When an electron orbits the cathode such that its drift velocity matches closely with the wave velocity of one of the resonant frequencies of the SWS, it will interact with the RF field. Those electrons that do not fall into one of these resonant frequencies continue to be emitted from the cathode and deliver energy to the RF environment, albeit inefficiently, providing the general background noise common to magnetron operation.

An electron in the vicinity of the RF wave, traveling at a greater velocity than that of the wave, will slowly pass through it and encounter the RF field leading the wave. This field, oriented toward the anode, counters the DC electric field and decelerates the

electron until it falls back in phase with the wave. Similarly, an electron traveling slower than the wave but still in its vicinity will encounter the trailing RF field, oriented toward the cathode, which will add to the DC electric field and will accelerate the electron back into phase with the RF wave. An electron outside of the wave will experience a similar effect where it will either be accelerated into the wave, if travelling faster than the wave, or decelerated until it falls into the anode or slows into the next wave, if travelling slower than the wave [8]. This effect is known as phase bunching [5] or phase focusing [8].

In a conventional magnetron, the sequence of positive to negative charge build up functions most effectively when it completes a full cycle every other resonance cavity. The attendant RF field then completes π full cycles as the wave orbits the cathode, hence the term π-mode.

Interestingly, while conventional magnetrons operate most effectively in the π-mode, the A6 relativistic magnetron instead tends to operate in the 2π-mode; that is, the electric fields for the dominant mode completes a full positive-to-negative-to-positive cycle in between each vane. This leads to a very different particle plot arrangement with a fully formed spoke occurring for each resonance cavity every cycle. The π-mode generally operates at less than half the efficiency of the 2π-mode.

A significant cause for this difference is the size of the A-K gap. As will be shown in Chapter 3, the cathode radius of the A6 magnetron must be decreased significantly before the π-mode consistently operates as the dominant frequency instead of the 2π-mode.

2.2 Detailed Explanation of Strapping

The SWS of the magnetron anode block can be modeled as an inductive-capacitive circuit with each vane effectively electrically isolated from those to either side so long as the distance between vanes is small compared with the wavelength of the resonant frequency. Collins [7] defines the requirements for this relation as

$$\frac{2\pi r_s}{N\lambda} < 1 \tag{3}$$

where r_s is the effective strap radius and N is the number of resonant cavities in the anode. Assuming that the effective strap radius is approximately equivalent to the physical radius, it can be seen that this inequality holds true for frequencies well above the 2π-mode in the A6 magnetron.

This isolation means the vanes are only weakly coupled to each other, providing minimal impact on what frequencies resonate predominantly in each vane. Each vane has multiple potential resonant frequencies; if the vanes lock in to different frequencies, mode competition will result. By providing a direct electrical connection between vanes, strapping enhances the coupling and reduces that mode competition. This can be modeled simply as shown in Fig. 2.1, adapted from Fig. 4.5 in [7] where L and C are the resonant cavity's inductance and capacitance and M is the mutual coupling between the cavities.

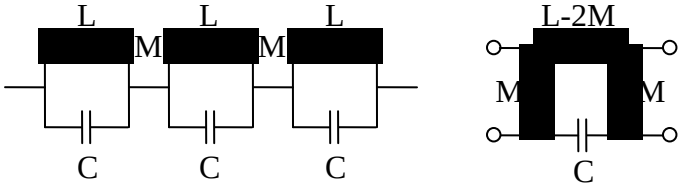

Figure 2.1. Schematic circuit of a chain of 4-terminal networks (left) and equivalent circuit (right) [7].

In the unstrapped case, M is typically small and provides minimal effect on the overall circuit. Collins showed through circuit theory that this circuit network will serve as a bandpass filter with cutoff frequencies of $\omega = 1/\sqrt{LC}$ and $\omega = 1/\sqrt{\mathrm{C(L-2M)}}$. Assuming that the cavity's inductance and capacitance cannot be altered easily, the mutual coupling is the only factor that can be readily adjusted; this is accomplished by the use of strapping.

Collins went on to show that, for the symmetric double-strapped resonator modeled as a sequence of 8-terminal networks, the critical terms can be related with the following equations.

$$\cos\psi_m = \cos\frac{2\pi s}{\lambda} + \frac{K_s}{2Z_{r_0}}\sqrt{\frac{\lambda^2}{\lambda_{r_0}^2} - 1}\left(\sin\frac{2\pi s}{\lambda}\right)\left(\tanh\frac{\pi h}{\lambda}\right)\sqrt{\frac{\lambda^2}{\lambda_{r_0}} - 1} \tag{4a}$$

$$\cos\psi_m = \cos\frac{2\pi s}{\lambda} + \frac{K_s}{2Z_{r_0}}\sqrt{\frac{\lambda}{\lambda_{r_0}^2} - 1}\left(\sin\frac{2\pi s}{\lambda}\right)\left(\mathrm{ctnh}\frac{\pi h}{\lambda}\right)\sqrt{\frac{\lambda^2}{\lambda_{r_0}} - 1} \tag{4b}$$

where $\cos\psi_m$ is the real component of the Euler's formula conversion of the wavelength for a given mode m; $2\pi s/\lambda$ is the electrical length of the strap; λ/λ_{r_0} is the ratio between the wavelength in question and the resonant wavelength of the cavity; h is the length of the anode, and $K_s/2Z_{r_0}$ is the relation between the wave guide impedance of the strap section and the impedance of the resonant cavity.

Equation 4a applies to symmetric modes, those corresponding to mode numbers that are integer multiples of π; Eq. 4b applies to the asymmetric modes, corresponding to non-integer multiples of π.

Given that the electrical length of the strap will remain constant and that the value of ψ_m is limited to certain discrete values based on its definition, it is apparent that

$K_s/2Z_{r_0}$ is the only variable that can be altered to adjust the wavelength of the resonant mode. This value, labeled as *k* in [7], is referred to as the weight of the strapping.

As k increases, the asymmetric mode wavelengths increase. The symmetric mode wavelengths will increase if $\cos\psi_m$ is greater than $\cos\frac{2\pi s}{\lambda_{r_0}}$ or decrease if it is less. However, the rate of increase will not be the same as the asymmetric mode wavelengths and enhanced mode separation is thus achieved in either case.

A similar derivation can be made for single-strapped systems based on a sequence of four-terminal networks with a similar result; specifically, the wavelength of the resonant modes is found to depend upon the weight of strapping. Collins noted, however, that mode separation is achieved much more slowly in this case as the weight of strapping is increased. The difference arises from the fact that the single strap is tied only to alternate vanes; there is a full resonant cavity between each strap connection. As the resonant wavelengths are increased, they eventually pass the cutoff wavelength of the cavity. The weight of strapping, when adjusted to account for this, reaches a point where the impedance of the strap coupling path approaches that of the resonant cavity itself. At this point, the impedances are roughly matched along parallel paths and cause a significant drop in the impedance of the circuit.

These results were derived originally for the conventional magnetron operating in the π-mode. In general, the mathematics should hold for the relativistic magnetron operating in either the π-mode or 2π-mode as the frequency regime is similar to the conventional magnetron and power is not explicitly addressed in this discussion.

CHAPTER 3 - SIMULATION STUDY

In this chapter, various methods of anode strapping are studied and compared with the traditional A6 anode endcap[1] design. The basic model of the A6 magnetron is described first followed by a brief discussion of the transparent cathode and then the changes for each configuration are explained. After the geometries are described, the simulation results are discussed, a look at the effect of certain strapping techniques on the electric fields in the magnetron is considered, and, lastly, the results are summarized.

Simulations for this study were performed using MAGIC3D, a three-dimensional fully electromagnetic, fully relativistic Finite Difference Time Domain (FDTD)/Particle-in-Cell (PIC) modeling tool developed by ATK-MRC [16]. Previous studies have shown good agreement between MAGIC3D simulation and experimental results [15]. All simulation runs for this study were performed on a custom-built personal computer using an Intel Core i7 920 processor clocked to 3.40 GHz, 6 GB of RAM and using Windows Vista Ultimate 64-bit with Service Pack 2.

3.1 Simulation Model

This section will discuss the simulation model used throughout this work, beginning with the basic A6 magnetron geometry and then discussing the transparent cathode that was used and the effects its use may have had on the simulation results.

3.1.1 Basic Magnetron Geometry

The basic model for this study was a standard A6 magnetron used in previous studies [17]. The A6 is characterized by several basic parameters as described by

[1] The anode endcap will be discussed in more detail in Section 3.2.1 below but should not be confused with the more common cathode endcap such as those discussed in [19], [23] and [26].

Palevsky and Bekefi [18] and summarized as follows: cathode radius 1.58 cm, anode radius 2.11 cm, cavity radius 4.11 cm, vane angular width 40°, cavity angular width 20°, anode vane length 7.2 cm, and a total of 6 anode vanes.

For this study, the magnetron was driven by a voltage pulse with a 1 ns risetime after which it maintained level amplitude of 350 kV up to the simulation duration of 40 ns as shown in Fig. 3.1.

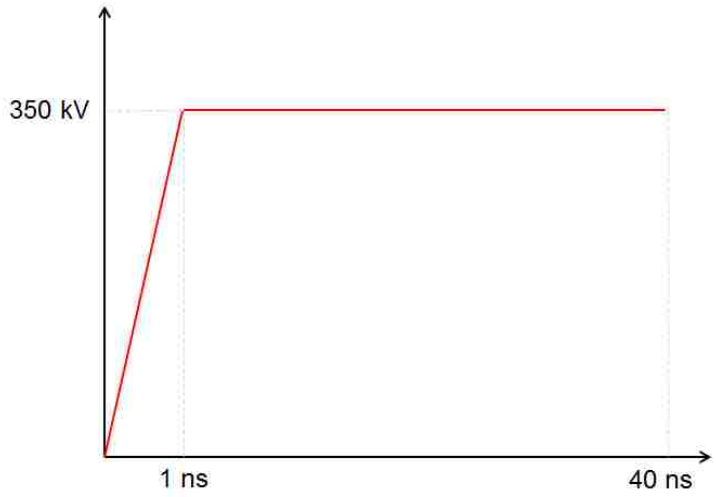

Figure 3.1. Shape of voltage pulse used in simulations.

Power is extracted through an output port located at the end of one of the resonating cavities. The outlet spans the length of the resonance cavity covering an angle of 10°, centered on the cavity. Measurements are taken in the region just beyond the end of the resonance cavity. Figure 3.2 shows the basic geometry in the r-phi plane midway along the A6 cavity as well as a rotated cutaway view of the double strap configuration detailed later.

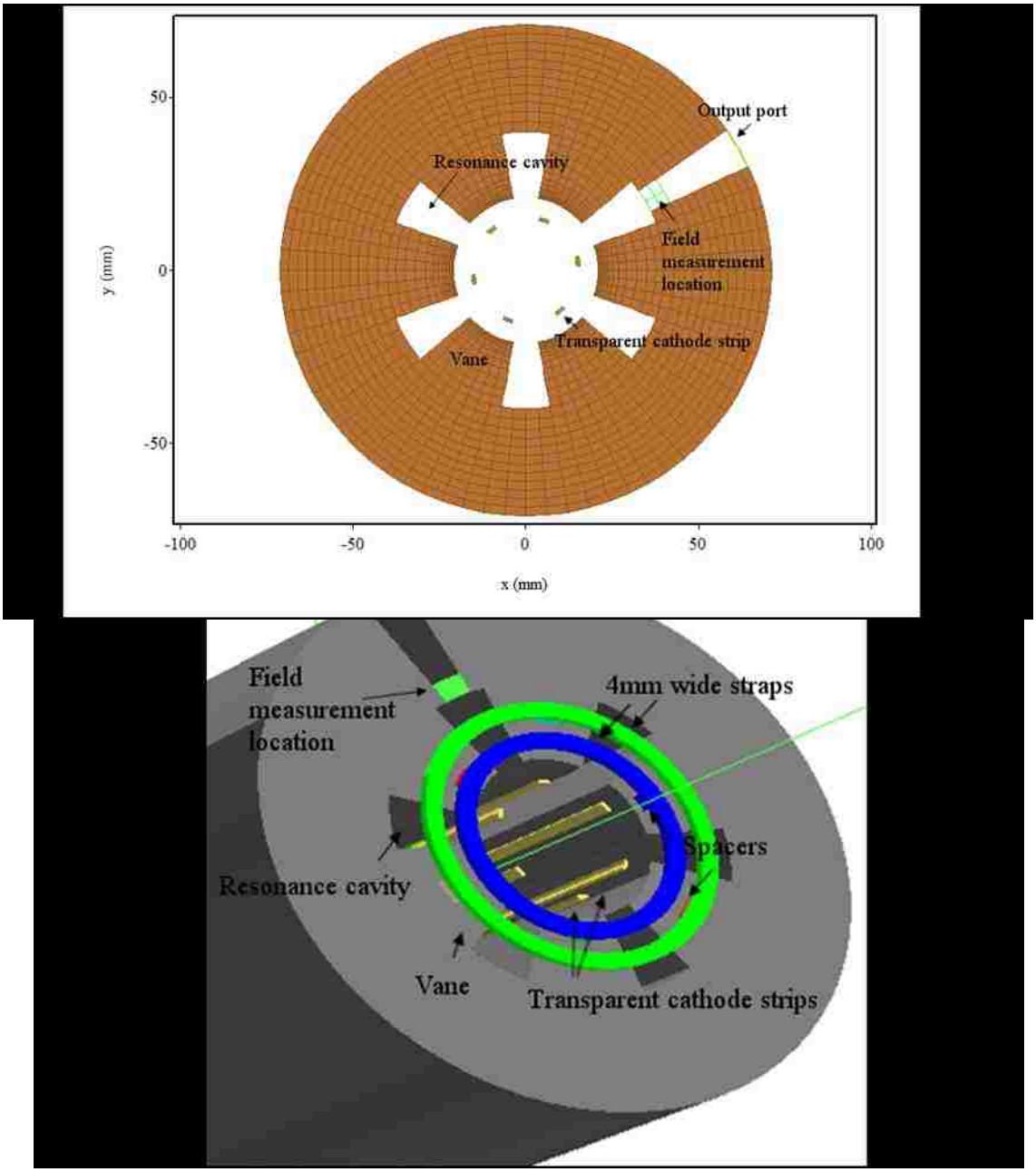

Figure 3.2. Geometry of the A6 magnetron in the r-phi plane midway down the length of the cavity (top) and cut view of the A6 magnetron showing the double ring configuration (bottom).

Several measurements were taken during each simulation. First, the power extracted at the output port was plotted against the simulation time for use as the primary comparison of overall effectiveness of each configuration. Second, a Fourier transform

of the output waveform was performed to determine the frequencies radiated and offer information regarding mode competition. Third, a field integral measurement of the energy deposited over the inner surface of the anode was taken to provide information on the total charge deposited on the anode. Fourth, a similar measurement was taken across the downstream end of the magnetron to determine the leakage current which, combined with the output power and the input voltage, was used to determine operating efficiency as an additional comparison of performance.

Sequences of simulations were performed for each configuration of the magnetron described below. Scans were performed at three different cathode radii to demonstrate the impact on mode competition by various configurations and due to the strong preference for operation in the 2π-mode demonstrated by the A6 magnetron. The cathodes used had inner/outer radii of 14.8/15.8 mm (standard for the A6 magnetron), 13.5/14.5 mm, and 12.5/13.5 mm. These sizes will generally be referred to as large, middle, and small radii, respectively, throughout the rest of this work. A sweep varying the magnetic field from 0.4-0.7 T in 0.02 T increments was conducted on each strap/cathode configuration. A study by Treado *et al.* on operating modes of the A6 magnetron used a solid cathode with a radius of 12.7 mm to force operation in the π-mode [19], which reinforced observations by Palevsky in his dissertation with the K8 magnetron [20] confirming that a large A-K gap is necessary for oscillation in the π-mode; unfortunately, the current work was well underway before that study was noted. This work did produce a similar observation that a much smaller cathode radius is necessary to force π-mode operation in the A6 magnetron.

For most of the simulation region, MAGIC was allowed to automatically select the resolution using the built-in AUTOGRID command as is recommended by the software developers. However, to ensure sufficient resolution in the interaction areas of interest, certain regions were set at higher resolution using the MARK command. The primary areas treated this way were the A-K gap and the regions at the end of the anode block where the straps were located. Simulations used between 108,000 and 190,000 cells depending on the geometry used.

3.1.2 Choice of Cathode

Typically, relativistic magnetrons use a uniform emission cylindrical cathode commonly referred to as a "solid cathode". Figure 3.3 is a photograph of a solid cathode that was used in experiments at UNM. When using a traditional solid cathode, the A6 typically operates in the 2π-mode and radiates primarily at 4.60 GHz. The π-mode radiates weakly at 2.34 GHz.

However, for this study, the transparent cathode as described in [17] and shown below in Fig. 3.4 was used as the baseline. Given the significant impact the transparent cathode has on the results following, a brief description is in order.

Figure 3.3. Photograph of a solid cathode used in UNM experiments.

Figure 3.4. Photograph of transparent cathode used in UNM experiments.

The transparent cathode, as proposed by Fuks and Schamiloglu [21], expanded upon by Bosman *et al.*[17] and experimentally demonstrated by Prasad *et al.*[22], effectively consists of several conducting bars extending from the cathode base into the body of the magnetron arranged circularly about the center axis, each bar offset by a few degrees from the nearest resonating cavity. This arrangement provides for cathode priming via electron pre-bunching around the cathode strips, which yields an initial predisposition to 2π-mode operation. In addition, the non-conducting center to the cathode changes the requirement for the azimuthal electric field $E_\theta = 0$ from occurring at r_c to occur instead at r = 0. This shift in boundary requirements allows for increased field amplitude in the electron sheath region, greatly accelerating oscillation buildup.

These advantages not only significantly reduced required simulation time but also significantly reduced the mode competition effects. However, as will be noted below, the A6 using the transparent cathode but with anode endcaps removed still demonstrated π-mode contamination, though at a reduced level from the solid cathode configuration.

3.2 Anode Modifications and Strap Configurations

This section describes the various forms of coupling links between neighboring and alternate resonators that were studied in this research.

3.2.1 Magnetron with Endcaps

Axial modes exist in magnetrons due to the finite length of the anode block. By placing metal endcaps on either side of the anode block one can electrically define its length and avoid axial mode competition. In a system that does not implement endcaps the electrical length is determined by the proximity of metallic objects. Axial mode purity is desirable in a magnetron that implements radial extraction of microwaves.

The traditional A6 magnetron includes endcaps completely blocking the anode vanes at either end. These anode endcaps are 9 mm thick. Figure 3.5 shows the location of the endcaps in blue. Note that throughout this work, the term "endcap" will refer to these anode endcaps. While the use of endcaps on cathodes has been studied extensively, for instance by Saveliev *et al.* [23] and Treado *et al.* [19], such a configuration was not attempted in the course of this study.

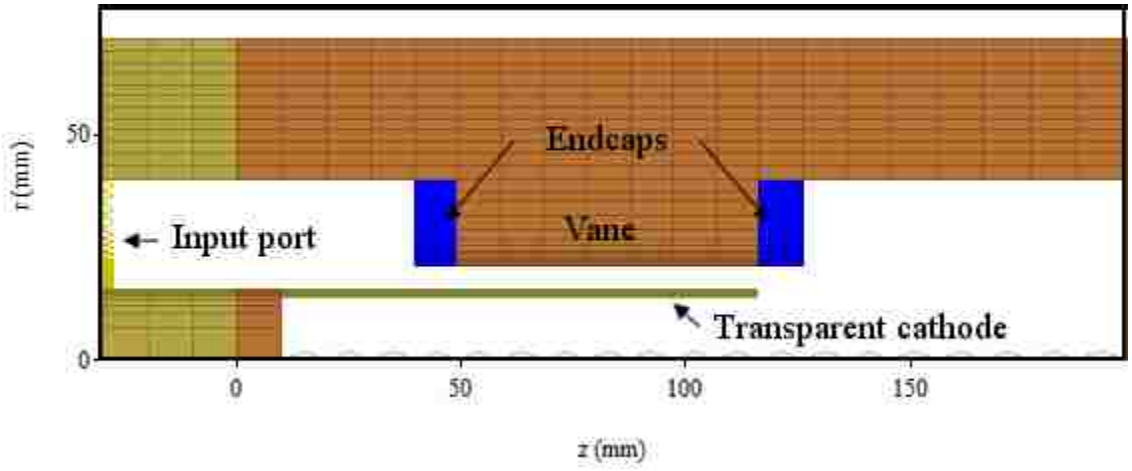

Figure 3.5. Geometry of endcap configuration in the r-z plane.

3.2.2 Magnetron without Endcaps

Simulations were also performed without endcaps or straps. This configuration removed the endcaps but left the rest of the magnetron the same as the endcap version; this served as the base configuration for the strapped versions. Essentially, where the traditional endcap version had solid plates covering both ends of the vanes, now those vanes are open. The terms "non-endcap" and "no endcap" are used to describe this configuration throughout this paper. Figure 3.6 highlights the location where the endcaps would be in a standard A6 magnetron. Note the area in Fig. 3.6 marked as 'vane' appears shorter than in Fig. 3.5; the apparent difference seen at this angle is simply the removal of the endcaps; the vane structure itself is unchanged.

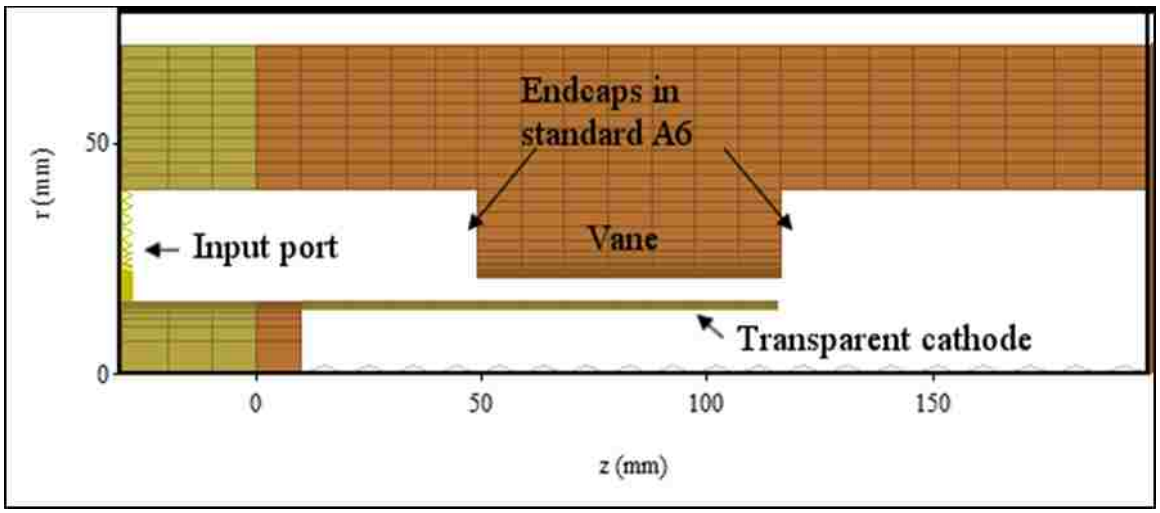

Figure 3.6. Geometry of non-endcap configuration in the r-z plane.

3.2.3 Magnetron with Single Strap

The magnetron without endcaps was modified to include a 4 mm wide conducting ring 1.8 mm above and below the anode block in the z-direction. The various studies conducted used rings with inner radii ranging from 21 mm to 35 mm in 2 mm increments.

The ring was tied to every other anode block using conductive connecting pieces that were defined as a conformal wedge 5° wide and 4 mm long in the radial direction. This shape was settled on after several attempts at defining a cylinder offset from the radial axis proved unworkable. Due to the wedge definition of the ring, the connectors varied from approximately 4 mm in width for the smaller radius rings and expanded to approximately 5 mm in width for the larger rings. The strap was tied to the same portion of the block on both the up- and down-stream sides. Figure 3.7 illustrates the geometry of the single strap configuration. An additional sequence of runs was made where the straps were tied to different sets of vanes up- and down-stream; this had minimal effect and is not reported further.

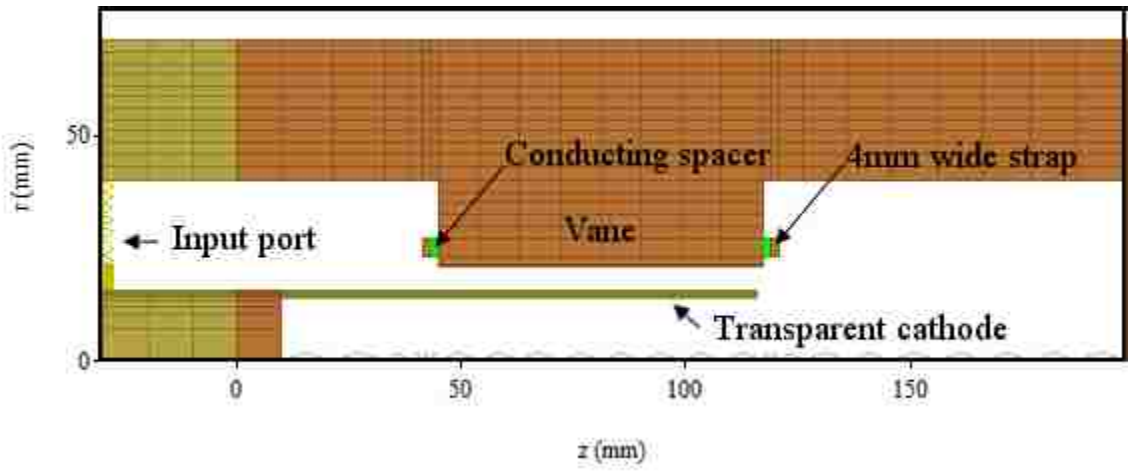

Figure 3.7. Geometry of single strap configuration in the r-z plane.

3.2.4 Magnetron with Double Straps

The double strap configuration used the same geometry as the single strap approach and added a second 4 mm ring with an inner radius 4 mm larger than the outer radius of the first. The connectors were defined similarly but were attached to the anode block offset 60° from the inner strap connections. Figure 3.8 illustrates the geometry of

this configuration. The lower portion of Fig. 3.2 above also demonstrates this configuration with an alternative view angle.

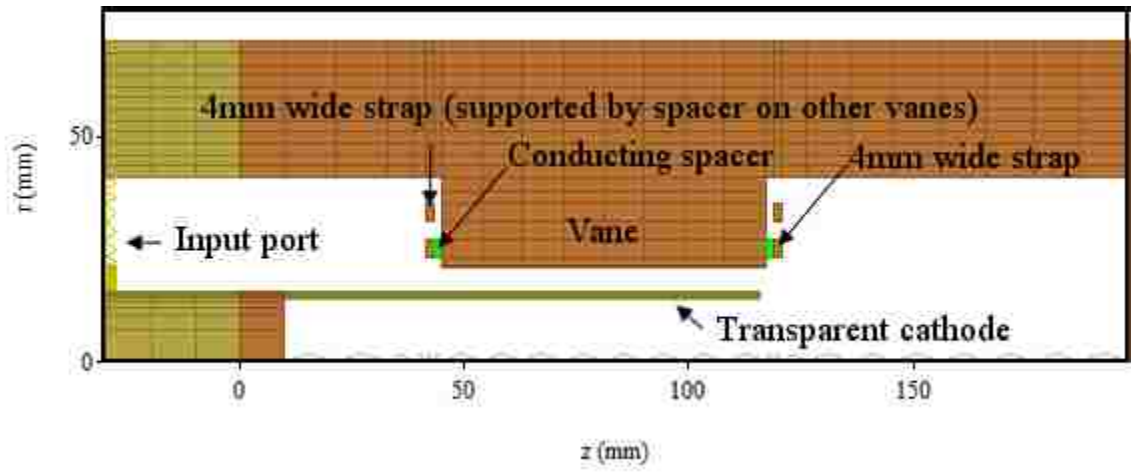

Figure 3.8. Geometry of double strap configuration in the r-z plane.

3.2.5 Magnetron with Wide Strap

The third strap configuration used a similar arrangement as the single strap version but widened the strap to 8, 10, and 12 mm with inner radii of 21 and 23 mm. The 10 mm strap with inner radius of 21 mm performed best of the configurations examined and is used as the representative sample for this approach.

Several variations of connectors were used, including single spacers as in the single strap configuration, paired spacers in a line extending in the radial direction, and using long spacers with the same width in the θ-direction as the other configurations but extending the radial length of the strap. The single spacer arrangement generally produced the best results in terms of output power and mode stability and would be the simplest physically-realizable approach. The single spacer arrangement is used in Fig. 3.9 to illustrate this configuration.

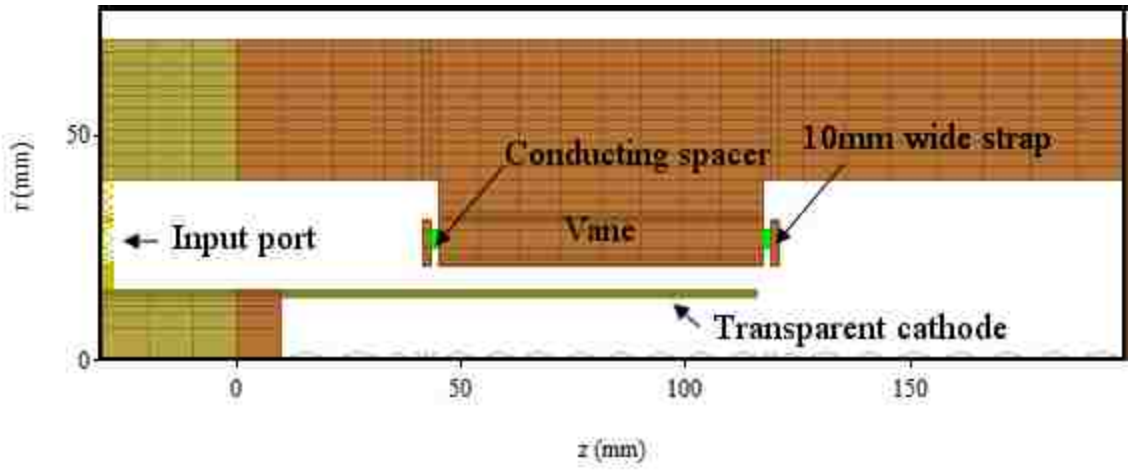

Figure 3.9. Geometry of 10-mm wide strap, 21 mm inner radius configuration in the r-z plane.

3.2.6 Magnetron with Recessed Straps

The fourth strap configuration attempted a strapping approach used in some non-relativistic magnetrons with the straps recessed into the anode block such as that shown in Fig. 6.2 of [5] or Fig. 4.2 of [7]. A channel was introduced into the anode block both up- and down-stream that was 4 mm deep and 1 mm wider than the straps required. The straps used were 1 mm or 2 mm wide with a 1 mm or 2 mm wide gap between them for a total of 4 variations examined. The straps were supported by connectors equal to the width of the strap with a height of 1.8 mm. Figure 3.10 demonstrates this configuration using the 1 mm wide straps with a 1 mm gap. Note that this configuration, while simulated, is unlikely to function adequately in reality due to arcing between the vanes and straps embedded in the channel.

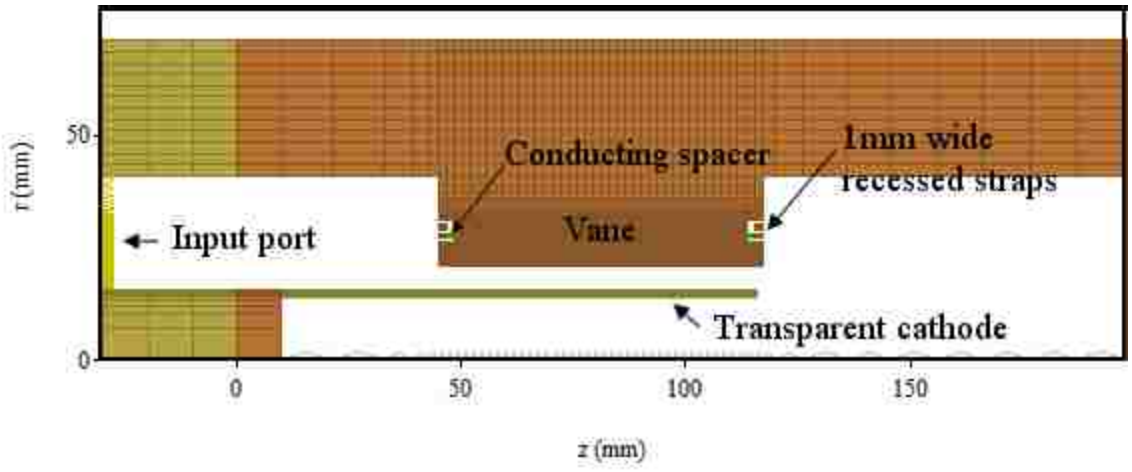

Figure 3.10. Geometry of recessed strap configuration in the r-z plane.

3.2.7 Magnetron with Single Strap Tied to All Vanes

After initial results on the previous configurations were obtained, the single strap version was modified to include a connection to all 6 vanes both up- and down-stream. This modification was attempted due to the preference the A6 magnetron showed for operation in the 2π-mode even when strapped to favor the π-mode. This configuration was only tested with inner/outer radii of 23/27 mm.

3.3 Simulation Results

Representative results for each of the configurations detailed are shown in the following sections with a discussion of performance compared against the endcap and non-endcap configurations. Factors presented are the maximum power output, average power output and the dominant frequencies radiated. Average power output was calculated using a simple arithmetic average of the instantaneous power outputs across the simulation period; this mitigated the effect seen in several simulations of a large output power spike that quickly dropped to a very low level as the simulation proceeded and provides a qualitative measure of the sustained performance for a given

configuration. Each section below includes a chart showing the maximum power output (blue line and diamonds), average power output (orange line and triangles), dominant frequency (red diamonds) and other significant frequencies (black diamonds) for each value of the magnetic field for the configurations discussed with the three cathode radii used. These figures also include a representative particle plot centered on the cathode in the r-θ plane at the middle of the extraction window to demonstrate mode pattern and stability. Also displayed for each configuration are power and frequency outputs for the largest cathode using a magnetic field of 0.66 T, the middle cathode using a magnetic field of 0.56 T, and the smallest cathode using a magnetic field of 0.42 T; these magnetic field values were the best performing for the endcap configuration. Other magnetic field values that yielded significant results are listed as well.

Analysis of the mode structure present during the simulations was achieved by visual inspection of the particle plots produced by MAGIC as well as evaluation of the frequency output graphs.

3.3.1 Magnetron with Endcaps

The endcap configuration was characterized by generally stable output power regardless of cathode radius. As the cathode radius decreased, the primary frequency decreased as well. In addition, the harmonic frequencies became more prevalent. Minor frequencies near the primary resonant frequency did not develop significantly.

With the largest cathode radius, the dominant frequency radiated at 4.20 GHz; Fig. 3.11 demonstrates a consistent dominant frequency across all values of the magnetic field tested and clear particle spokes on the particle plot, indicating stable 2π-mode operation. Figure 3.12 shows the smooth power output profile generated and the

comparatively clean frequency output of the endcap configuration. Figure 3.13 and Fig. 3.14 show similar information for the middle cathode radius with similar overall performance but with greater dependence on magnetic field variations. The middle cathode radius radiated most effectively at 4.17 GHz.

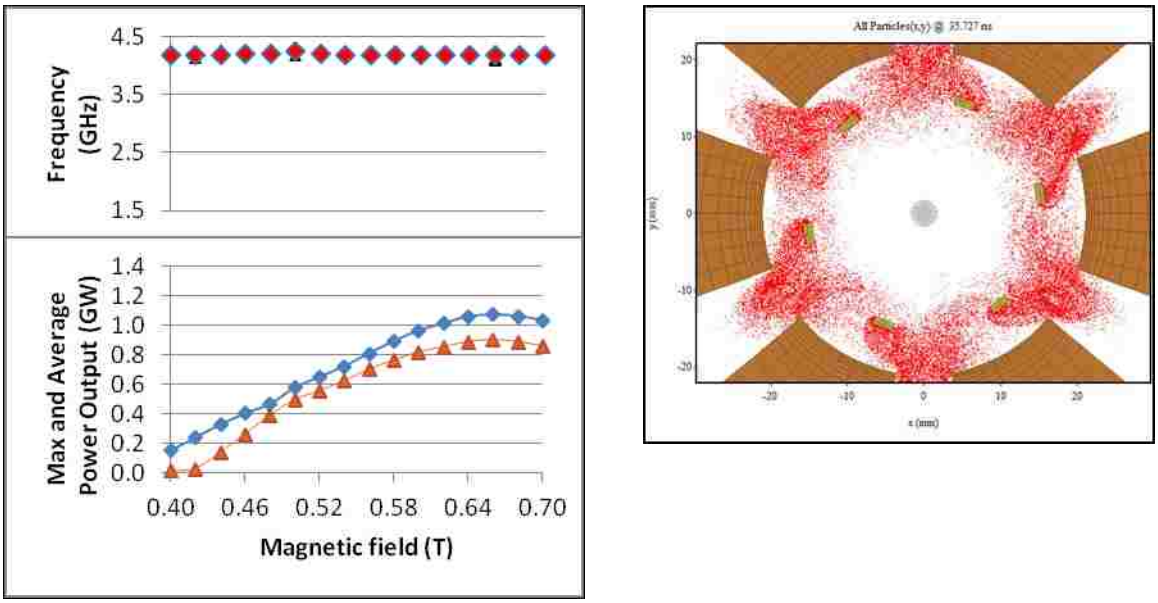

Figure 3.11. Power output and primary frequency as a function of magnetic field (left) and particle plot at saturation with magnetic field of 0.66 T demonstrating 2π-mode operation (right) for magnetron with endcaps and large cathode radius. Note the clear spoke formation indicating stable 2π-mode operation.

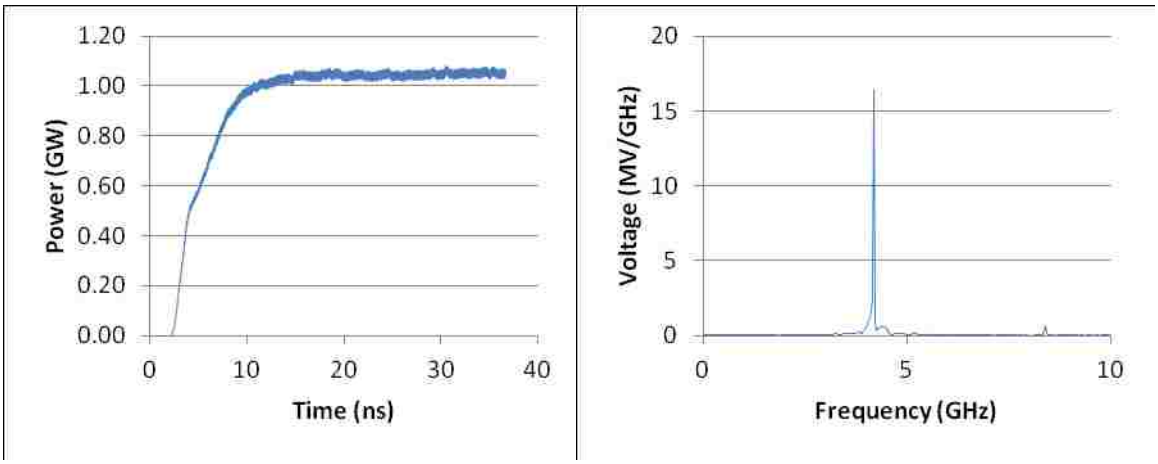

Figure 3.12. Output power (left), frequency spectrum of the RF signal (right) for magnetron with endcaps at a magnetic field of 0.66 T and large cathode radius.

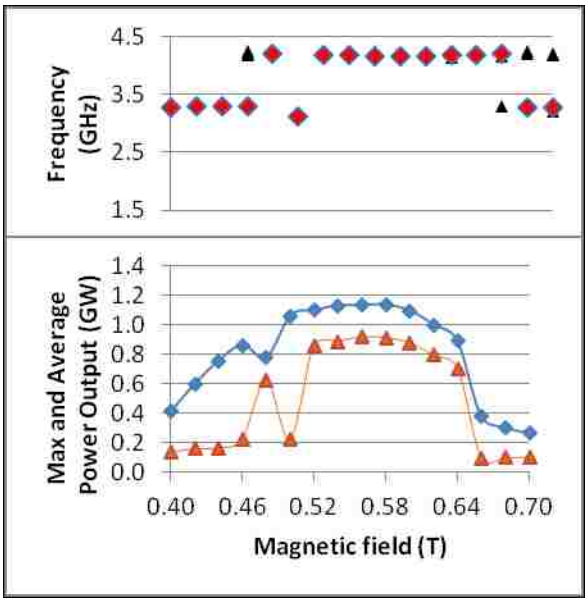

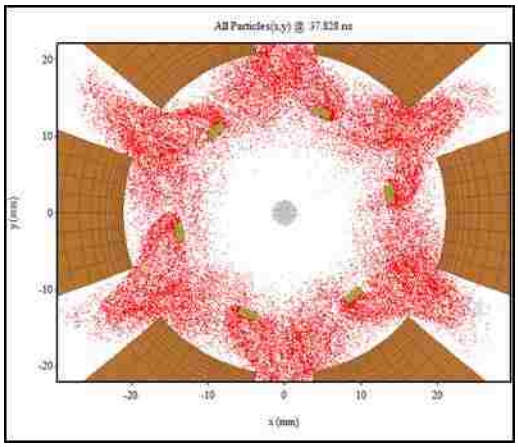

Figure 3.13. Power output and primary frequency by magnetic field (left) and particle plot at saturation with a magnetic field of 0.56 T demonstrating 2π-mode operation (right) for magnetron with endcaps and middle cathode radius.

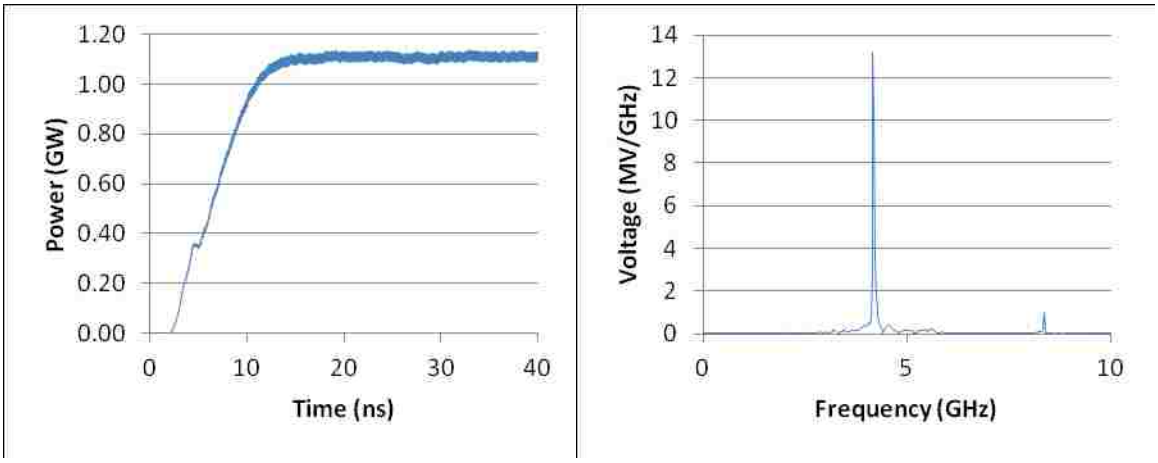

Figure 3.14. Output power (left), frequency spectrum of the RF signal (right) for magnetron with endcaps at a magnetic field of 0.56 T and middle cathode radius.

Figure 3.15 and Fig. 3.16 demonstrate the same information for the smallest cathode radius. Note that, in this case, the magnetron operated in π-mode at 3.32 GHz. Also note the magnetron radiated poorly with a magnetic field above 0.54 T; although the

peak output power occurred at 0.56 T, the average output at that point was less than half that produced at 0.42 T.

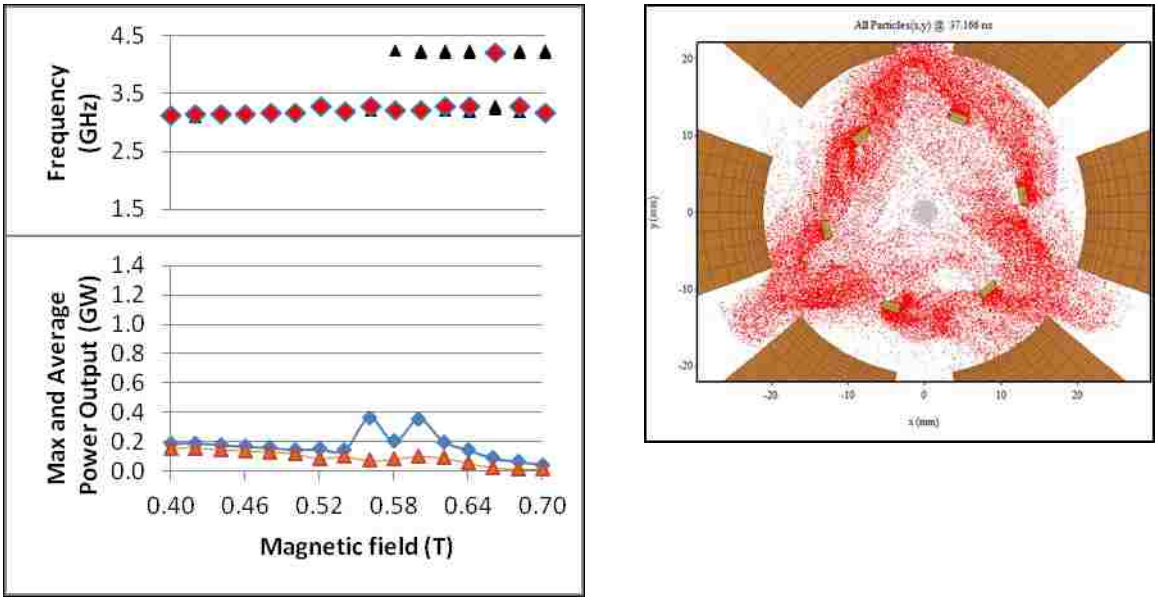

Figure 3.15. Power output and primary frequency as a function of magnetic field (left) and particle plot at saturation with a magnetic field of 0.42 T demonstrating π-mode operation (right) for magnetron with endcaps and small cathode radius.

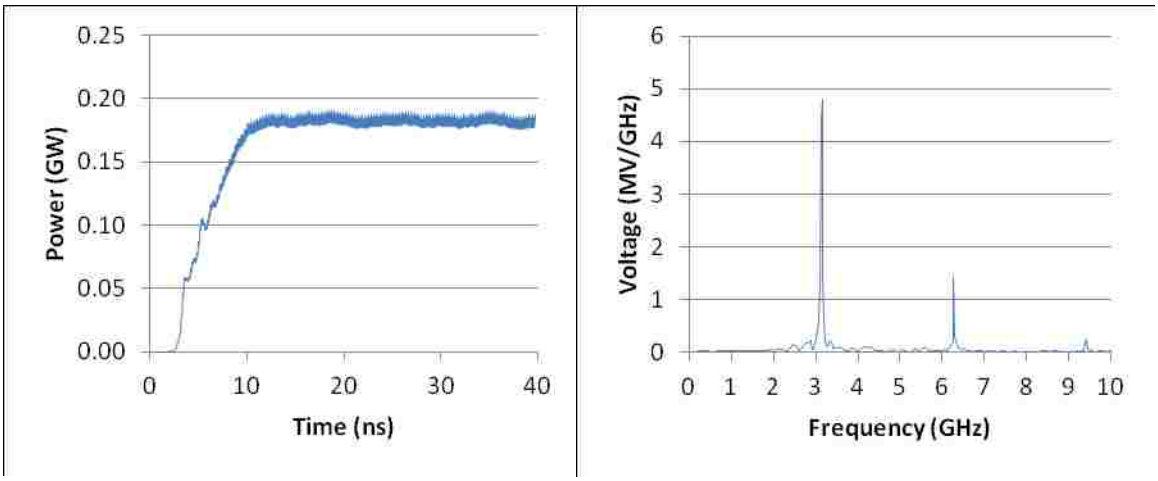

Figure 3.16. Output power (left), frequency spectrum of the RF signal (right) for magnetron with endcaps at magnetic field of 0.42 T and small cathode radius.

Given the generally consistent output across various cathode radii, it is clear why the anode-endcap configuration is the currently preferred geometry for A6 magnetrons.

3.3.2 Magnetron without Endcaps

Not surprisingly, the non-endcap configuration showed significantly worse performance when using the smaller cathode radii, producing between 40-60% of the output power of the endcap configuration due to significantly increased mode competition, comparable to observations noted by Palevsky and Bekefi [18] and Treado *et al.* [19].

Perhaps more interesting, the largest cathode radius evaluated showed only a 7% decrease in power output while operating at a noticeably lower 3.75 GHz with only slightly more minor frequencies, primarily at π-mode, in evidence; this is considered more of a testament to the effectiveness of the transparent cathode rather than a fault of either previous research or this work. Figure 3.17 indicates a much greater dependence on magnetic field for effective operation with this configuration; the decreased power performance corresponds exactly with points where the π-mode was either dominant or at least radiated significantly. Note in Fig. 3.18 the increase in ringing on the power output as well as the more pronounced frequency interference from additional mode operation, particularly around 2.5 GHz.

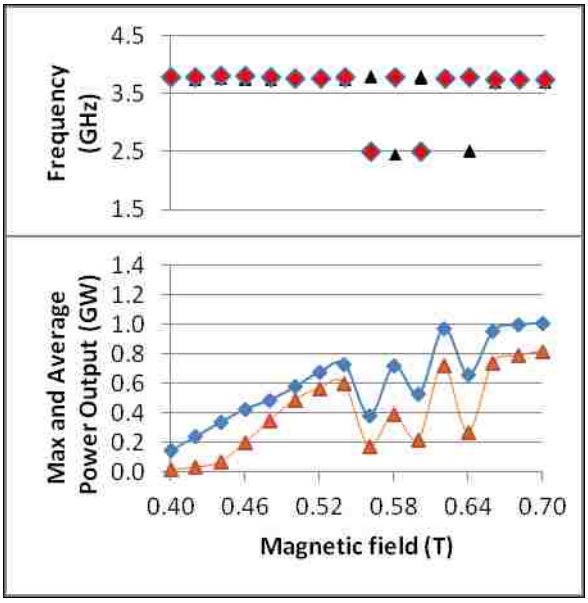

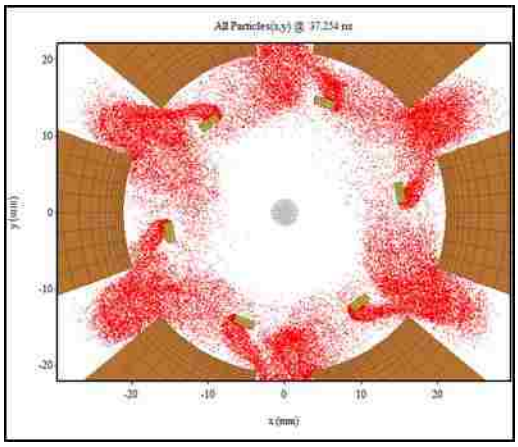

Figure 3.17. Power output and primary frequency as a function of magnetic field (left) and particle plot at saturation with a magnetic field of 0.66 T demonstrating 2π-mode operation (right) for magnetron without endcaps and large cathode radius.

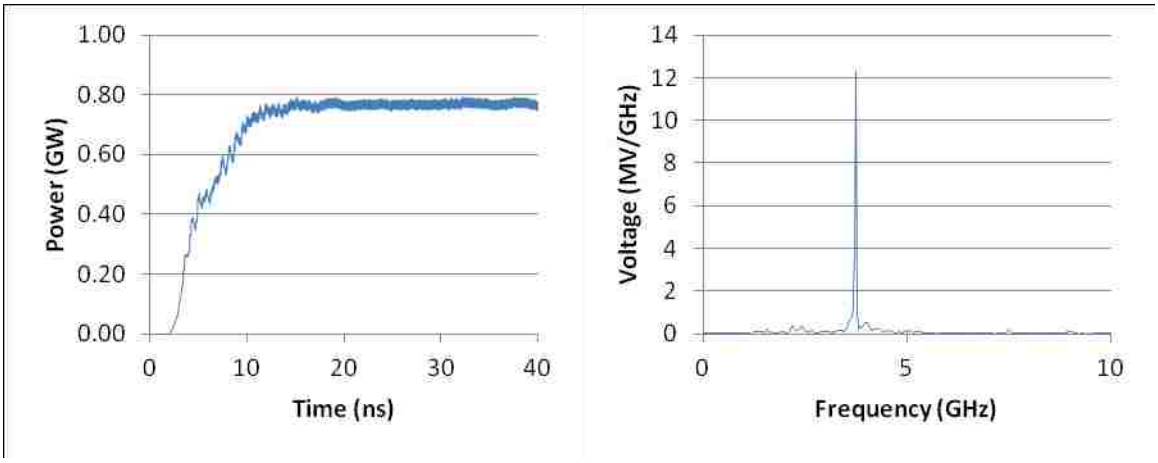

Figure 3.18. Output power (left), frequency spectrum of the RF signal (right) for magnetron without endcaps at magnetic field of 0.66 T and large cathode radius.

As seen in Fig. 3.19, the non-endcap configuration was only marginally effective at radiating at 0.56 T with the middle cathode radius. The extreme mode competition around the primary frequency indicated in Fig. 3.20 provides an indication as to the cause.

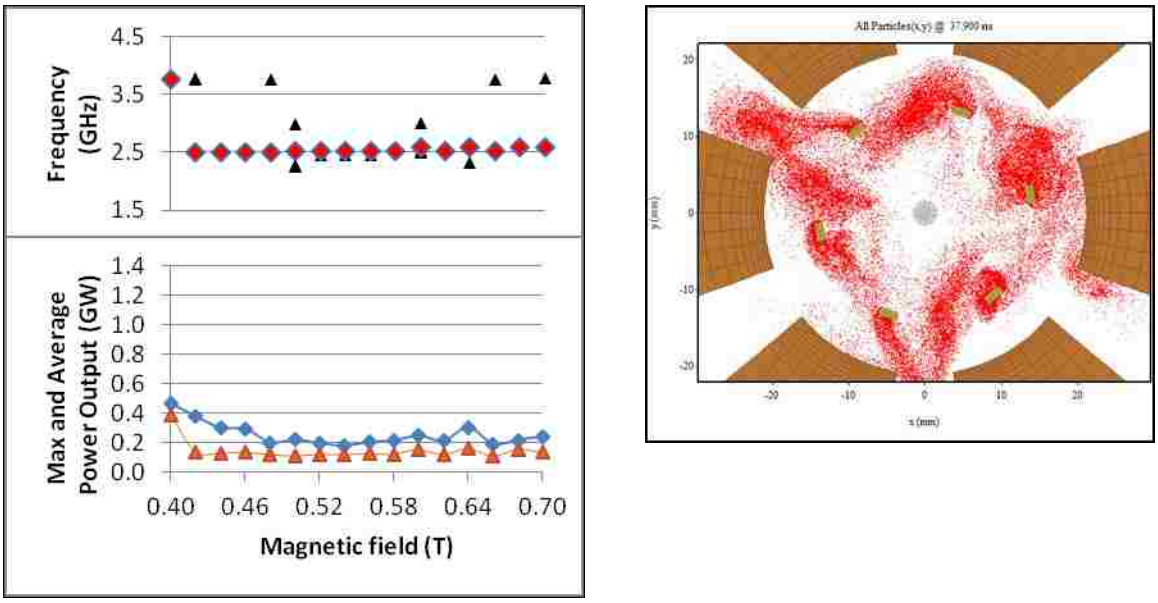

Figure 3.19. Power output and primary frequency as a function of magnetic field (left) and particle plot at saturation with a magnetic field of 0.56 T demonstrating contaminated π-mode operation (right) for magnetron without endcaps and middle cathode radius.

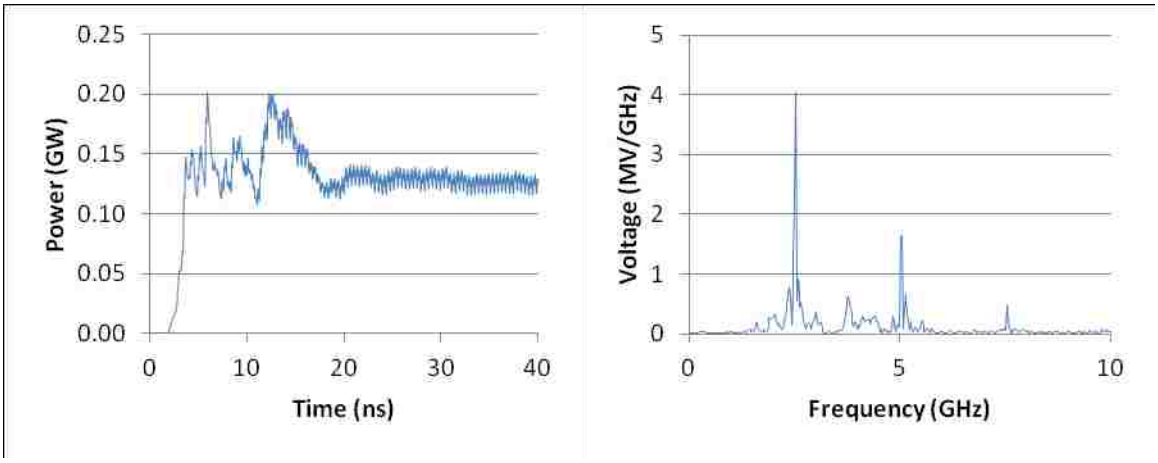

Figure 3.20. Output power (left), frequency spectrum of the RF signal (right) for magnetron without endcaps at a magnetic field of 0.56 T and middle cathode radius.

Figure 3.21 shows the performance of the non-endcap configuration with the smallest cathode radius. While the output is minimal, it outperformed the endcap configuration above 0.54 T. Figure 3.22 shows the expected mode competition decreasing performance.

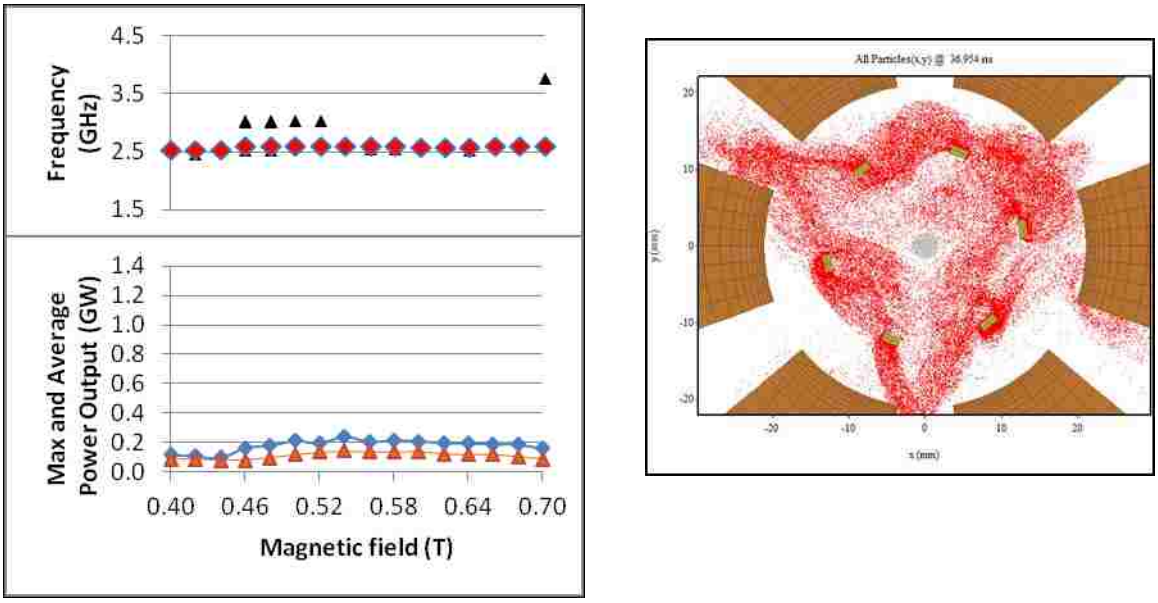

Figure 3.21. Power output and primary frequency as a function of magnetic field (left) and particle plot at saturation with a magnetic field of 0.42 T demonstrating contaminated π-mode operation (right) for magnetron without endcaps and small cathode radius.

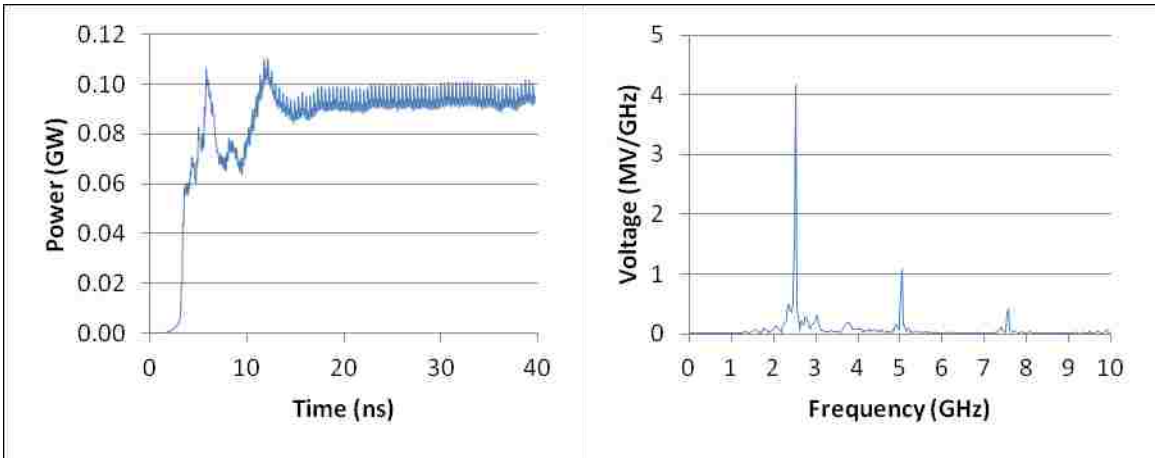

Figure 3.22. Output power (left), frequency spectrum of the RF signal (right) for magnetron without endcaps at a magnetic field of 0.42 T and small cathode radius.

3.3.3 Magnetron with Single Strap

The single strap configuration displayed generally similar output results to those of the endcap configuration in terms of stable power output. The largest radius cathode radiated at 3.95 GHz, approximately midway between the endcap and non-endcap

configurations, and generated about 5% more power than the endcap configuration with nearly the same efficiency. Figure 3.23 indicates that this configuration reacted similarly to the endcap when magnetic field levels were varied. Examining Fig. 3.24 reveals that the primary signal is radiated with a slightly greater bandwidth than the endcap displayed but otherwise contained similar amounts of mode competition. Considering the increased power levels generated, this may indicate an acceptable trade-off depending on requirements for future magnetron development.

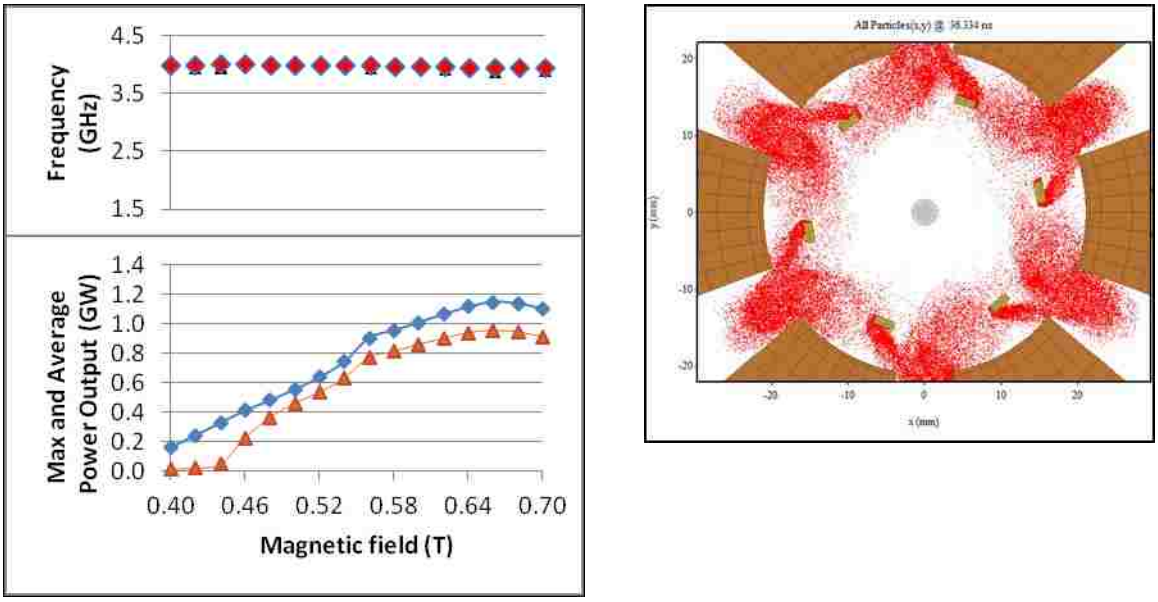

Figure 3.23. Power output and primary frequency as a function of magnetic field (left) and particle plot at saturation with a magnetic field of 0.66 T demonstrating 2π-mode operation (right) for magnetron with a single strap with inner and outer radii of 23 mm and 27 mm, respectively, and large cathode radius.

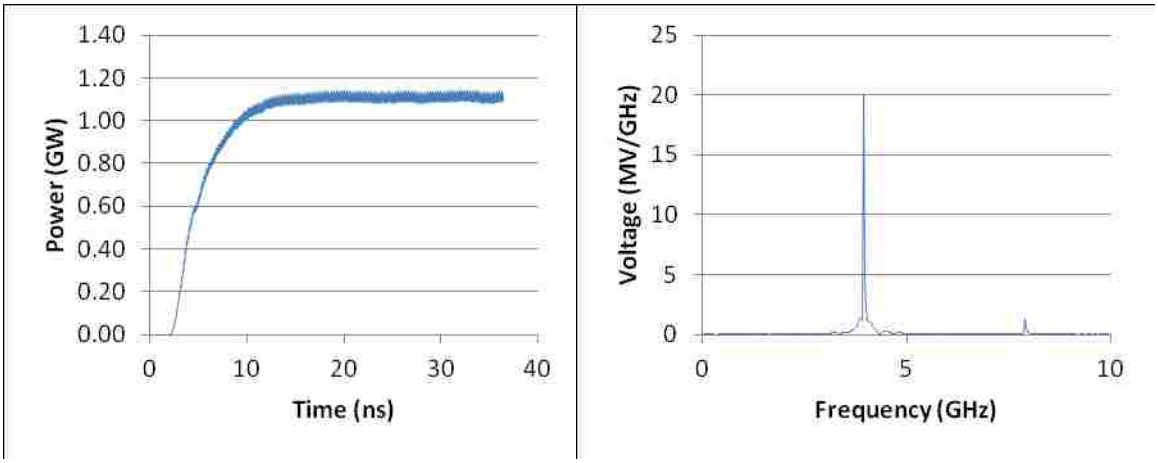

Figure 3.24. Output power (left), frequency spectrum of the RF signal (right) for magnetron with a single strap with inner and outer radii of 23 mm and 27 mm, respectively, at a magnetic field of 0.66 T and large cathode radius.

The middle cathode radius radiated 5% less power with 2% less efficiency than the endcap configuration at 3.95 GHz but nearly 2.5 times the non-endcap configuration. As shown in Fig. 3.25, the single strap configuration presented a much smoother response to varied magnetic field values than the non-endcap configuration. Figure 3.26 indicates comparable levels of mode competition to the endcap at the same magnetic field value.

With the smallest cathode radius, the single strap arrangement did not effectively radiate at 0.42 T as shown in Fig. 3.27, yielding only a third of the power of the endcap version at 3.00 GHz with 3% efficiency. Figure 3.28 indicates significant mode competition, similar to the non-endcap configuration.

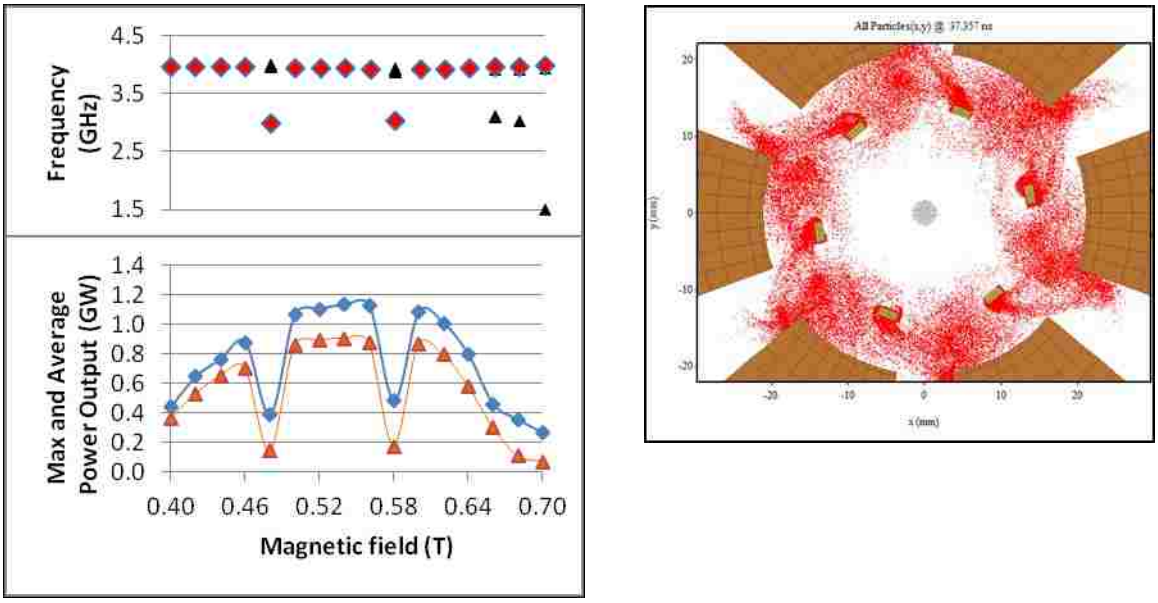

Figure 3.25. Power output and primary frequency as a function of magnetic field (left) and particle plot at saturation with a magnetic field of 0.56 T demonstrating 2π-mode operation (right) for magnetron with a single strap with inner and outer radii of 23 mm and 27 mm, respectively, and middle cathode radius.

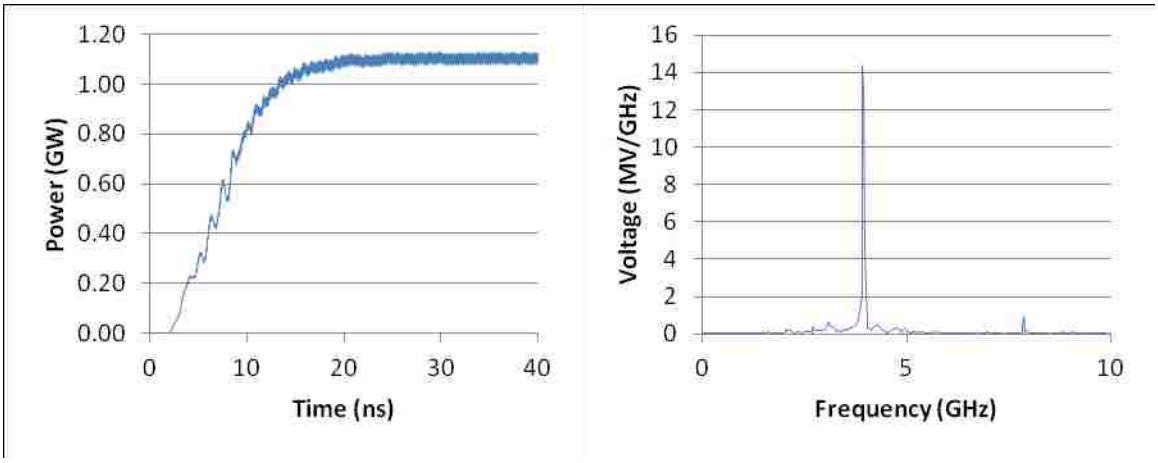

Figure 3.26. Output power (left), frequency spectrum of the RF signal (right) for magnetron with a single strap with inner and outer radii of 23 mm and 27 mm, respectively, at a magnetic field of 0.56 T and middle cathode radius.

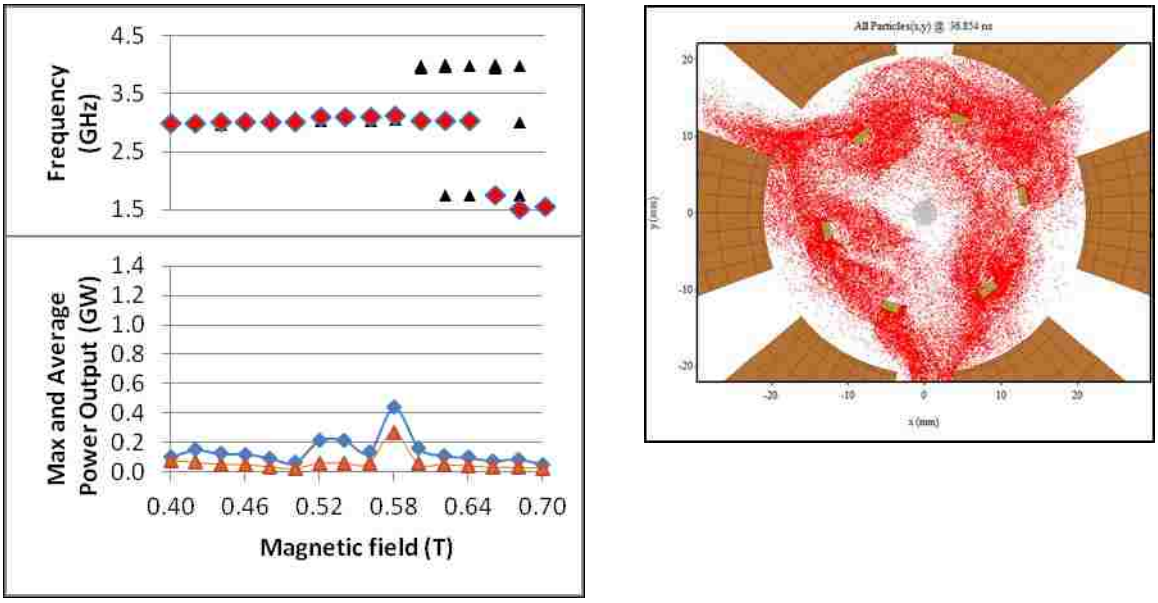

Figure 3.27. Power output and primary frequency as a function of magnetic field (left) and particle plot at saturation with a magnetic field of 0.42 T demonstrating contaminated π-mode operation (right) for magnetron with a single strap with inner and outer radii of 23 mm and 27 mm, respectively, and small cathode radius.

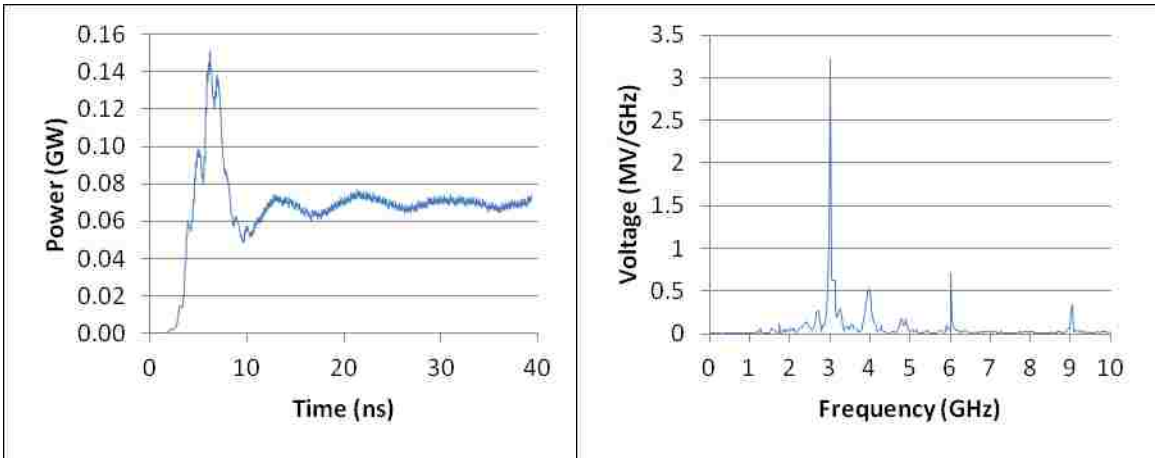

Figure 3.28. Output power (left), frequency spectrum of the RF signal (right) for magnetron with a single strap with inner and outer radii of 23 mm and 27 mm, respectively, at a magnetic field of 0.42 T and small cathode radius.

While those output characteristics may be interesting, the magnetic field sweeps indicated that those magnetic field values were not optimum for the strapped configuration with the smallest cathode. When operating in configurations where mode competition becomes a more significant problem such as the smallest cathode radius, the

single strap configuration radiated best with a magnetic field of 0.58 T, producing an average power 28% higher than the endcap configuration's peak at 0.42 T with 5% greater output efficiency at 3.12 GHz. Figure 3.29 indicates significant mode competition still exists but at a lower frequency compared to the 0.42 T case.

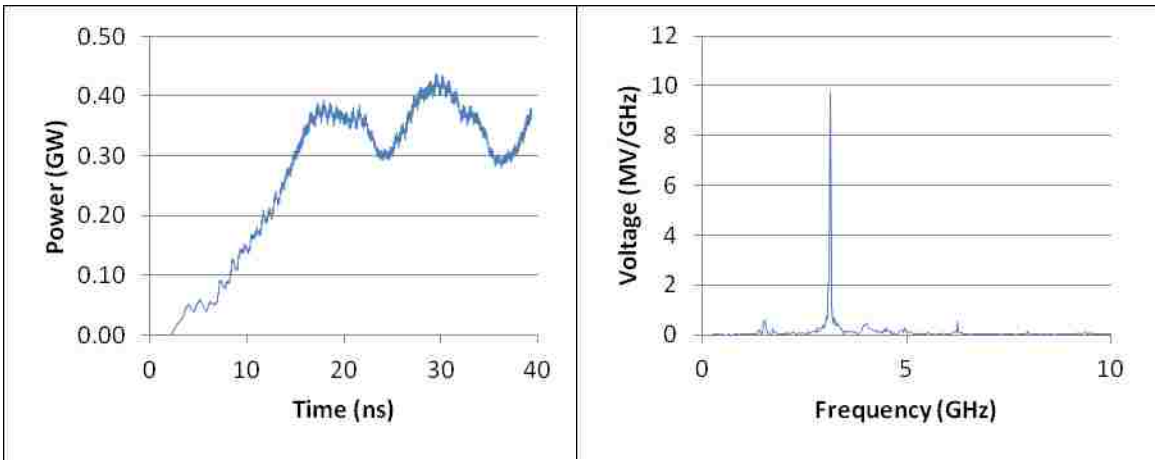

Figure 3.29. Output power (left), frequency spectrum of the RF signal (right) for magnetron with a single strap with inner and outer radii of 23 mm and 27 mm, respectively, at a magnetic field of 0.58 T and small cathode radius.

3.3.4 Magnetron with Double Straps

The double strap geometry displayed slightly greater power output than the single strap configuration with slightly lower dominant frequencies. As shown in Fig. 3.30, the largest cathode radius radiated at 3.87 GHz and produced 12% higher average power output than the endcap configuration with a 1% higher operating efficiency. Figure 3.31 indicates significantly reduced mode competition compared to the single strap configuration providing mode competition levels comparable to the endcap as shown earlier in Fig. 3.12.

The middle cathode radius operated at the same frequency but only produced 3% higher power than the endcap with no significant change to efficiency. Figure 3.32

shows the similar peak performance but also indicates a strong dependence on magnetic field values; note the approximately 60% reduction in peak power output at 0.58 T for this configuration compared to 0.56 T and 0.60 T. Figure 3.33 shows minor mode competition beginning to appear, both in the frequency FFT plot with the small peak at 1.5 GHz as well as the slight ringing on the power output.

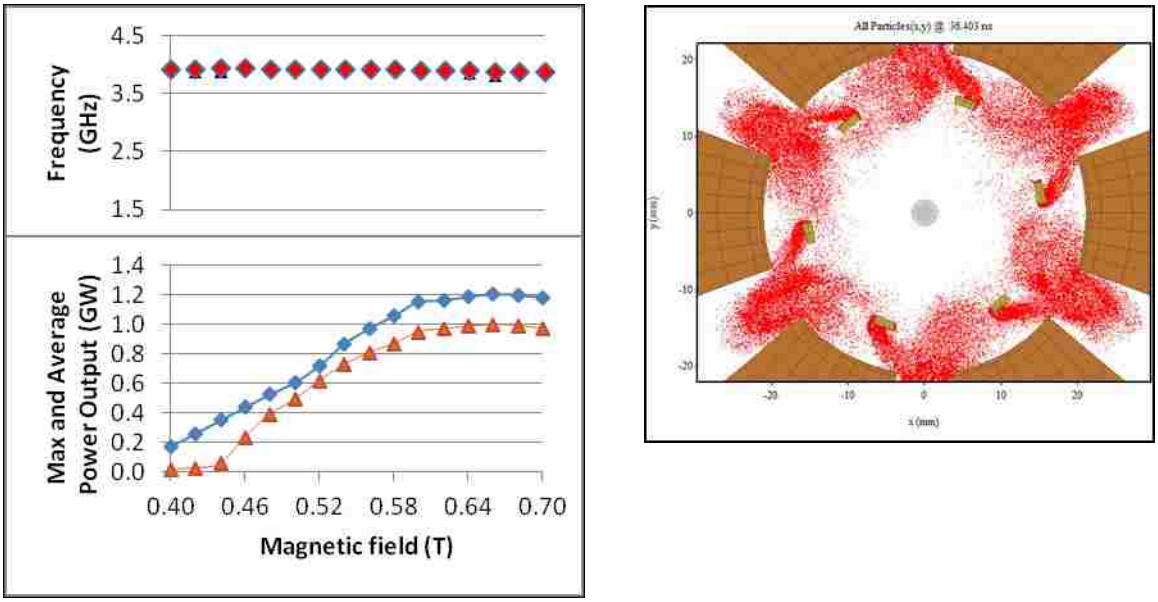

Figure 3.30. Power output and primary frequency as a function of magnetic field (left) and particle plot at saturation with a magnetic field of 0.66 T demonstrating 2π-mode operation (right) for magnetron with two straps, the first with inner and outer radii of 23 mm and 27 mm, respectively, and the second with inner and outer radii of 31 mm and 35 mm, respectively, and large cathode radius.

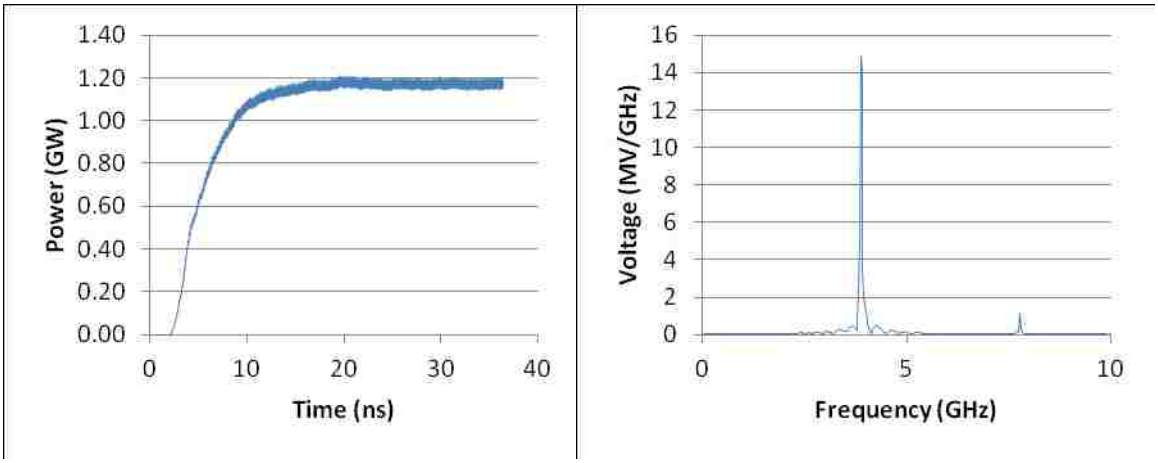

Figure 3.31. Output power (left), frequency spectrum of the RF signal (right) for magnetron with two straps, the first with inner and outer radii of 23 mm and 27 mm, respectively, and the second with inner and outer radii of 31 mm and 35 mm, respectively, at a magnetic field of 0.66 T and large cathode radius.

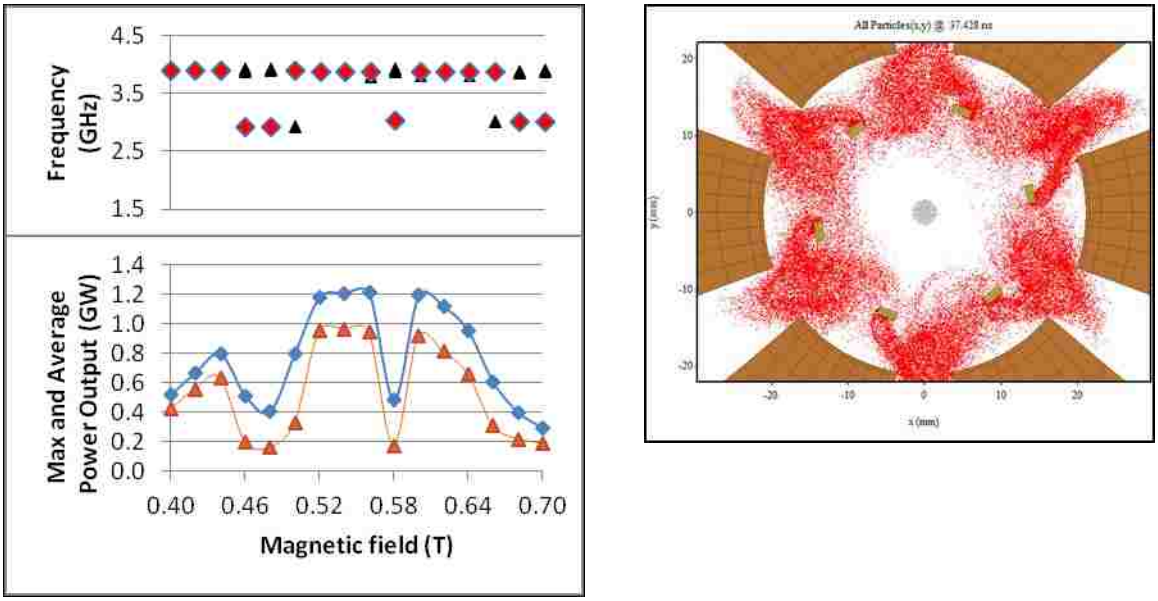

Figure 3.32. Power output and primary frequency as a function of magnetic field (left) and particle plot at saturation with a magnetic field of 0.56 T demonstrating mildly contaminated 2π-mode operation (right) for magnetron with two straps, the first with inner and outer radii of 23 mm and 27 mm, respectively, and the second with inner and outer radii of 31 mm and 35 mm, respectively, and middle cathode radius.

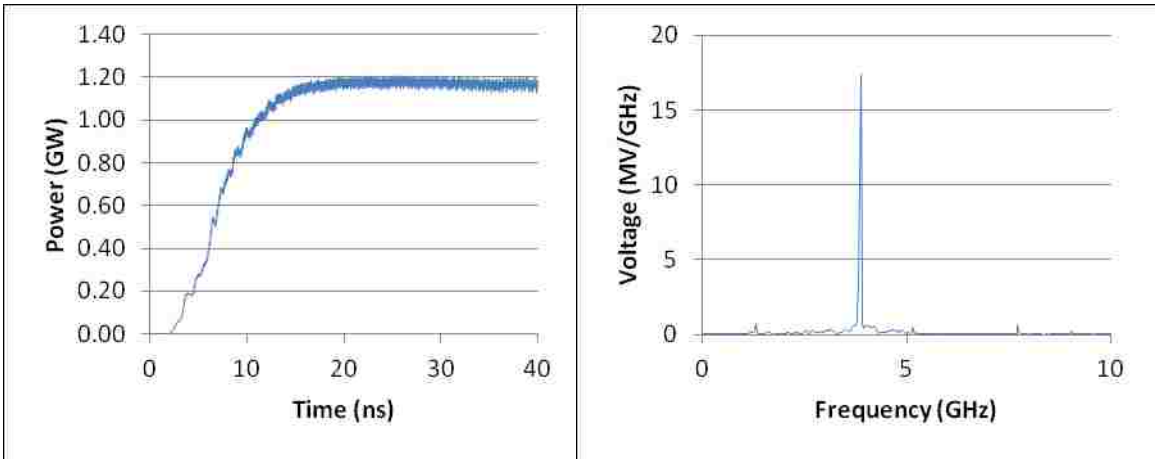

Figure 3.33. Output power (left), frequency spectrum of the RF signal (right) for magnetron with two straps, the first with inner and outer radii of 23 mm and 27 mm, respectively, and the second with inner and outer radii of 31 mm and 35 mm, respectively, at a magnetic field of 0.56 T and middle cathode radius.

The smallest cathode radius performed extremely poorly with the magnetic field of 0.42 T, achieving only 50% of the power output of the endcap configuration at 2.95 GHz with 10% lower efficiency. The particle plot in Fig. 3.34 shows the π-mode mingled with several other degenerate modes resulting in this poor performance; Fig. 3.35 shows the other frequencies that are competing. However, it should be noted that 0.42 T was one of the worst performing magnetic field value for this configuration.

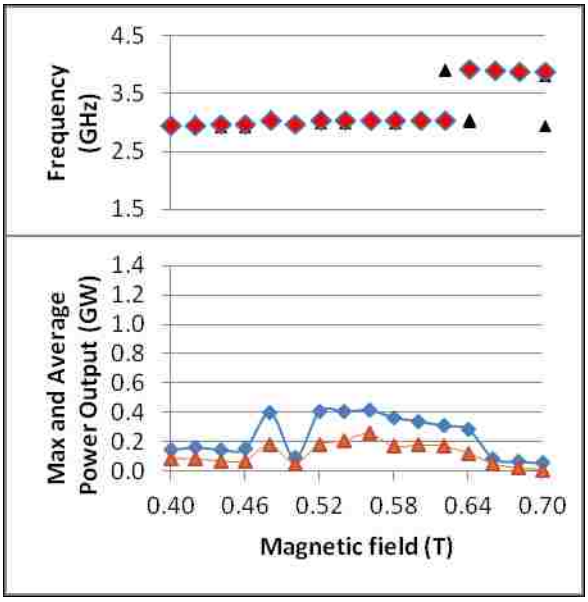

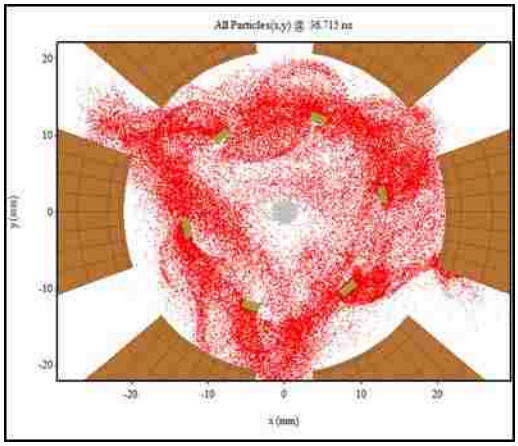

Figure 3.34. Power output and primary frequency as a function of magnetic field (left) and particle plot at saturation with a magnetic field of 0.42 T demonstrating contaminated π-mode operation (right) for magnetron with two straps, the first with inner and outer radii of 23 mm and 27 mm, respectively, and the second with inner and outer radii of 31 mm and 35 mm, respectively, and small cathode radius.

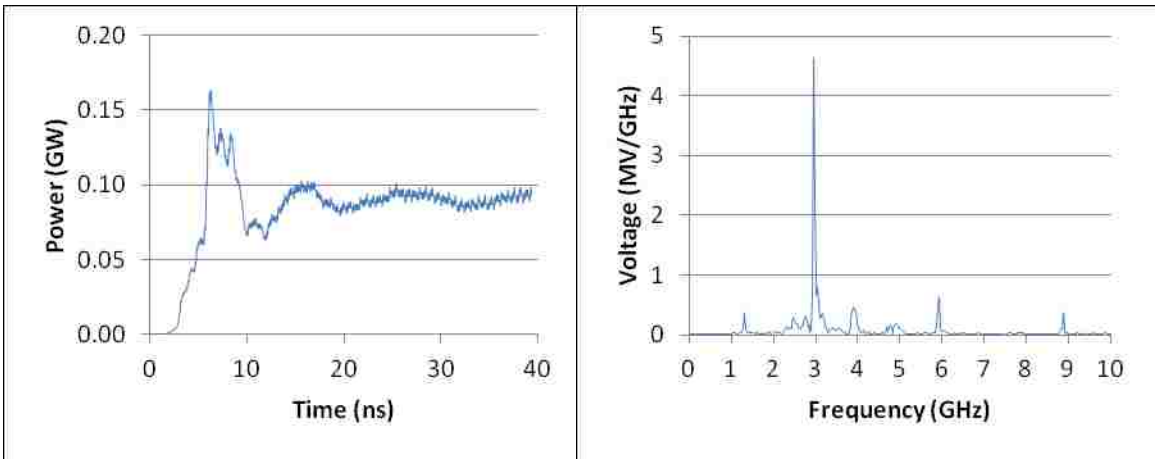

Figure 3.35. Output power (left), frequency spectrum of the RF signal (right) for magnetron with two straps, the first with inner and outer radii of 23 mm and 27 mm, respectively, and the second with inner and outer radii of 31 mm and 35 mm, respectively, at a magnetic field of 0.42 T and small cathode radius.

When operated with a magnetic field of 0.56 T, the double strap configuration with the small cathode achieved a 22% increase in output power with 3% higher efficiency at 3.05 GHz. The power and frequency output graphs are shown below in Fig. 3.36.

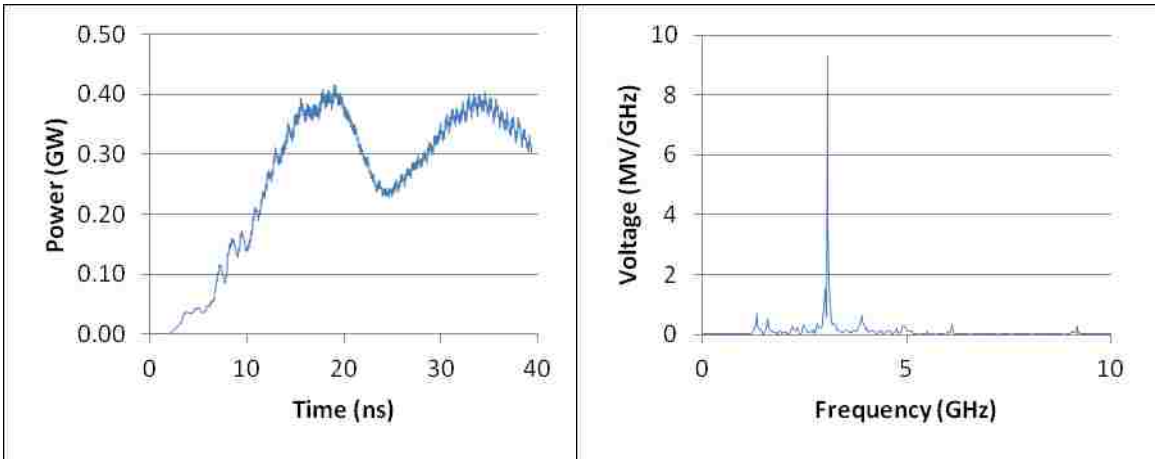

Figure 3.36. Output power (left), frequency spectrum of the RF signal (right) for magnetron with two straps, the first with inner and outer radii of 23 mm and 27 mm, respectively, and the second with inner and outer radii of 31 mm and 35 mm, respectively, at a magnetic field of 0.56 T and small cathode radius.

3.3.5 Magnetron with Wide Strap

The wide strap configuration closely matched the endcap configuration with the large cathode radius, perhaps not surprisingly considering how generally similar this configuration is to the endcap itself. Although the primary frequency radiated at 3.97 GHz, the average power output and efficiency were nearly identical. Figure 3.37 shows the generally similar response to magnetic field. Figure 3.38 also shows a similar FFT as the endcap configuration; compare against Fig. 3.12.

The comparison to the endcap configuration quickly deteriorated with the smaller radius cathodes. The middle radius cathode operating at 0.56 T radiated at 3.00 GHz and yielded only 18% of the average power output. As seen in Fig. 3.39, though, the middle radius cathode showed widely varying results depending on the magnetic field employed. Figure 3.40 shows the presence of at least one strongly competing frequency.

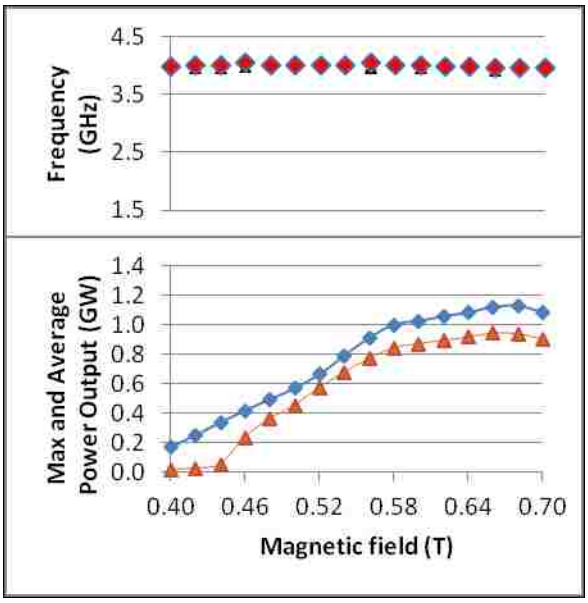

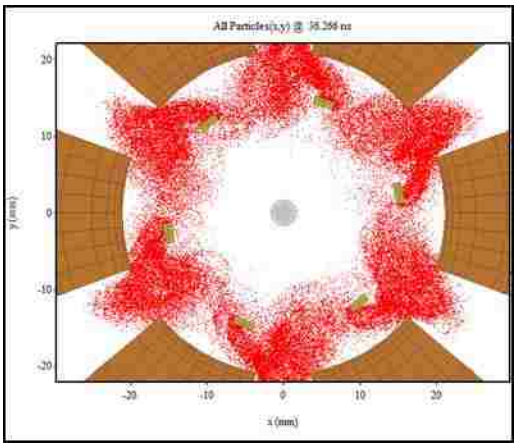

Figure 3.37. Power output and primary frequency as a function of magnetic field (left) and particle plot at saturation with a magnetic field of 0.66 T demonstrating 2π-mode operation (right) for magnetron with a single wide strap with inner and outer radii of 21 mm and 31 mm, respectively, and large cathode radius.

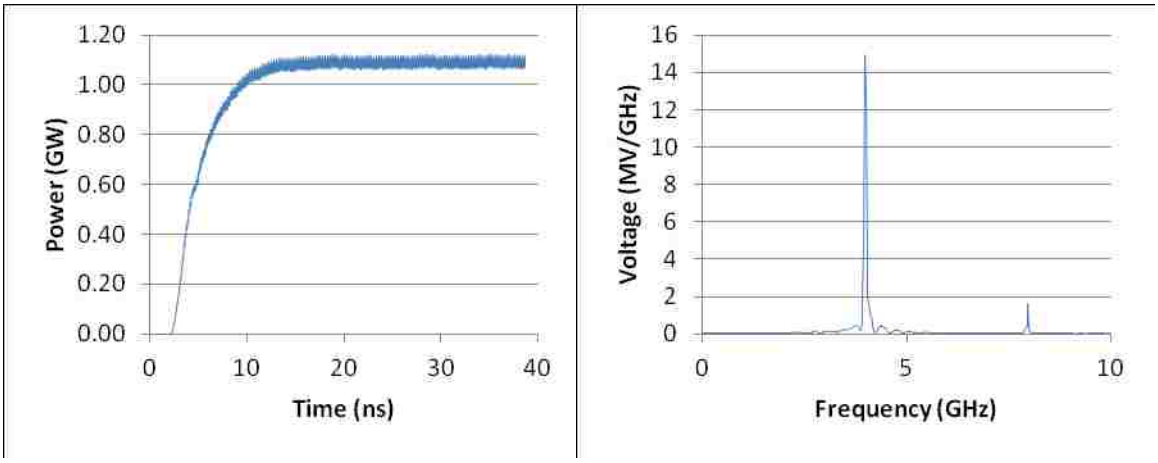

Figure 3.38. Output power (left), frequency spectrum of the RF signal (right) for magnetron with a single wide strap with inner and outer radii of 21 mm and 31 mm, respectively, at a magnetic field of 0.66 T and large cathode radius.

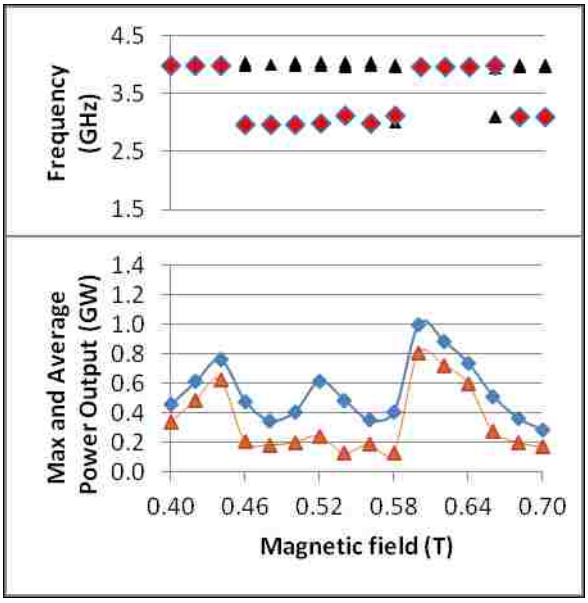

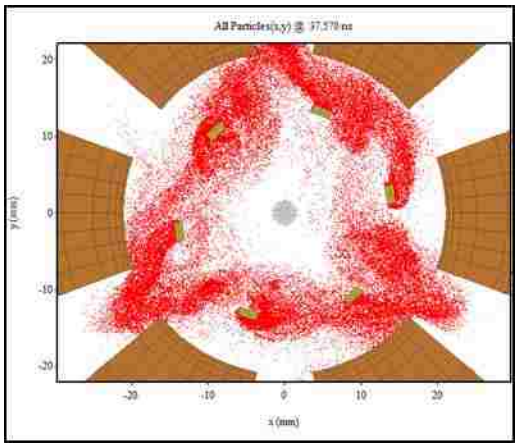

Figure 3.39. Power output and primary frequency as a function of magnetic field (left) and particle plot at saturation with a magnetic field of 0.56 T demonstrating π-mode operation (right) for magnetron with a single wide strap with inner and outer radii of 21 mm and 31 mm, respectively, and middle cathode radius.

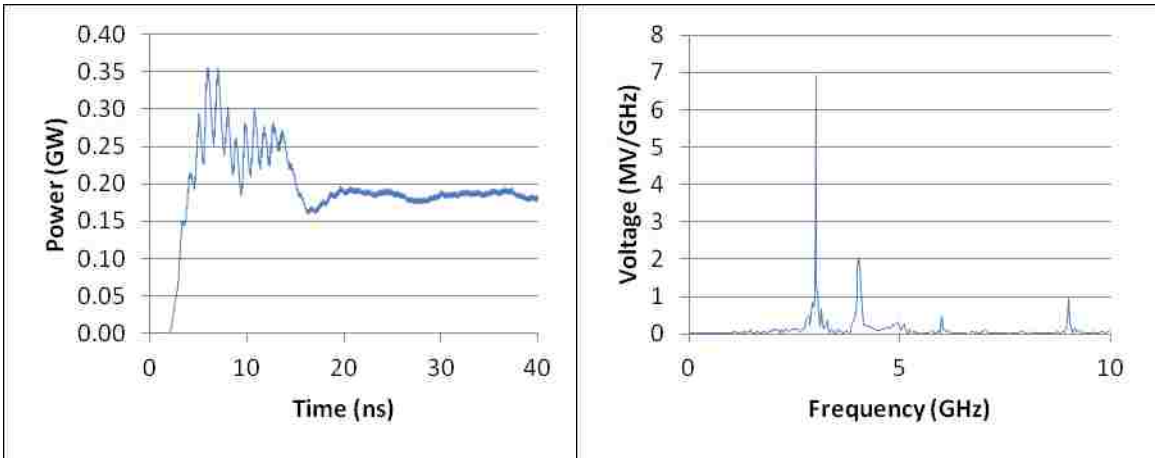

Figure 3.40. Output power (left), frequency spectrum of the RF signal (right) for magnetron with a single wide strap with inner and outer radii of 21 mm and 31 mm, respectively, at magnetic field of 0.56 T and middle cathode radius.

The small radius cathode also radiated at 3.00 GHz but produced 50% of the average power output at 10% less efficiency than the endcap configuration. Figure 3.41 indicates that this cathode radius did not radiate efficiently for most of the magnetic fields

investigated; however, Fig. 3.42 shows that for what radiation was generated, there was fairly little mode competition.

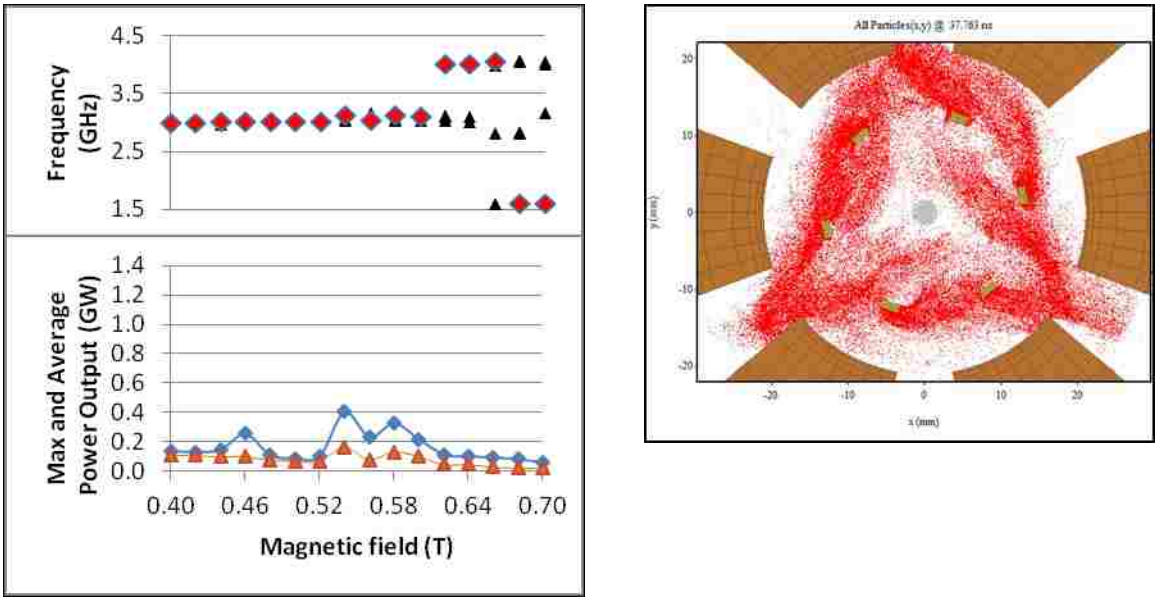

Figure 3.41. Power output and primary frequency as a function of magnetic field (left) and particle plot at saturation with a magnetic field of 0.42 T demonstrating π-mode operation (right) for magnetron with a single wide strap with inner and outer radii of 21 mm and 31 mm, respectively, and small cathode radius.

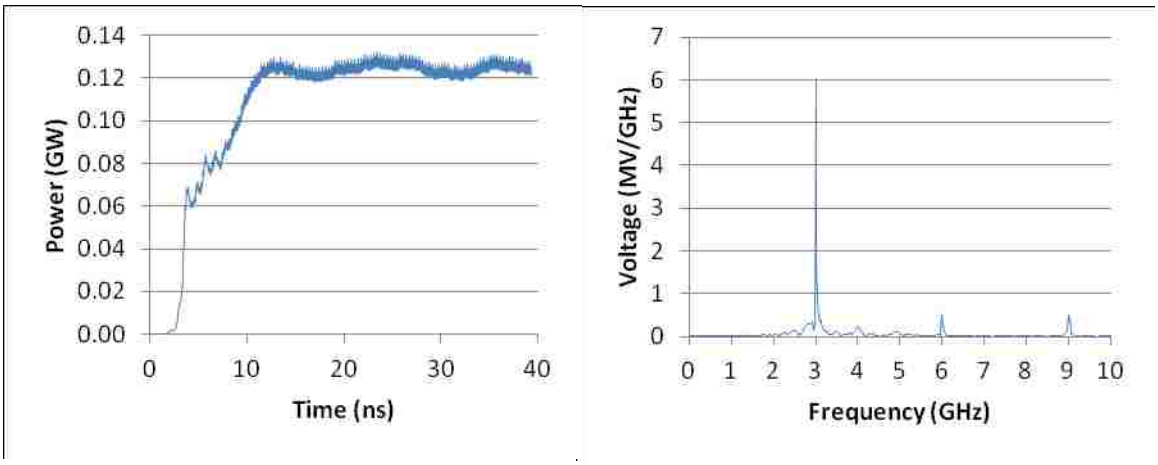

Figure 3.42. Output power (left), frequency spectrum of the RF signal (right) for magnetron with a single wide strap with inner and outer radii of 21 mm and 31 mm, respectively, at a magnetic field of 0.42 T and small cathode radius.

3.3.6 Magnetron with Recessed Straps

The recessed strap configuration demonstrated relatively consistent performance above 0.58 T with the largest cathode radius as shown in Fig. 3.43; Fig. 3.44 shows the relatively clean frequency spectrum generated for this configuration. However, the recessed strap configuration operated at a 10% lower output power and 2% lower efficiency for both the largest and middle cathode radius configurations compared to the endcap configuration; both cathode radii radiated at 3.90 GHz.

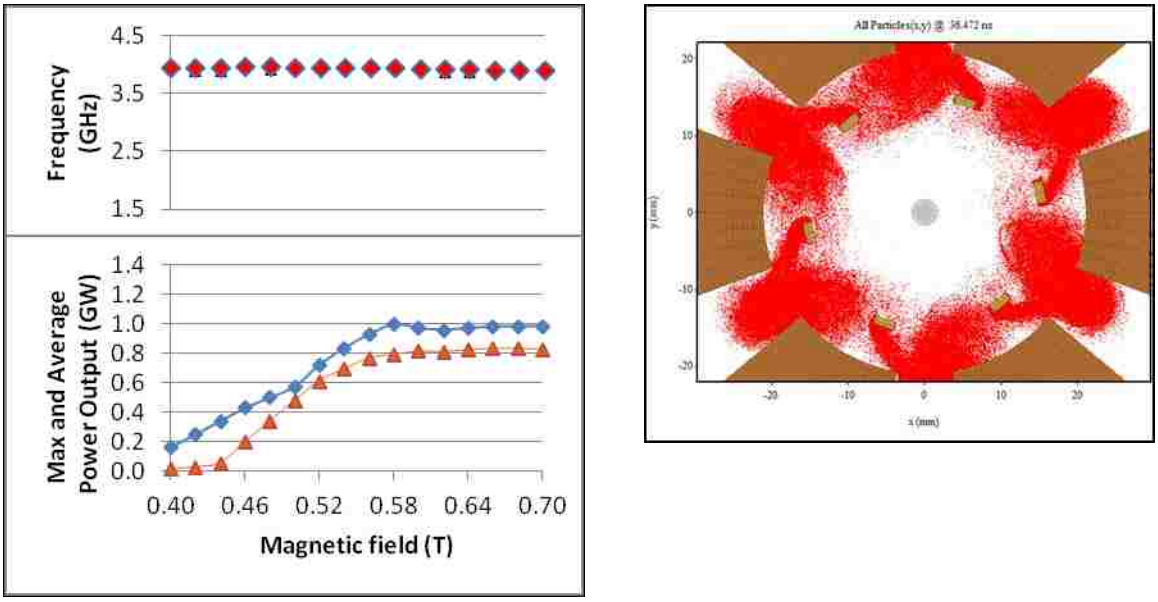

Figure 3.43. Power output and primary frequency as a function of magnetic field (left) and particle plot at saturation with a magnetic field of 0.66 T demonstrating 2π-mode operation (right) for magnetron with 2 recessed straps, the first with inner and outer radii of 27 mm and 28 mm, respectively, and the second with inner and outer radii of 29 mm and 30mm, respectively, and large cathode radius.

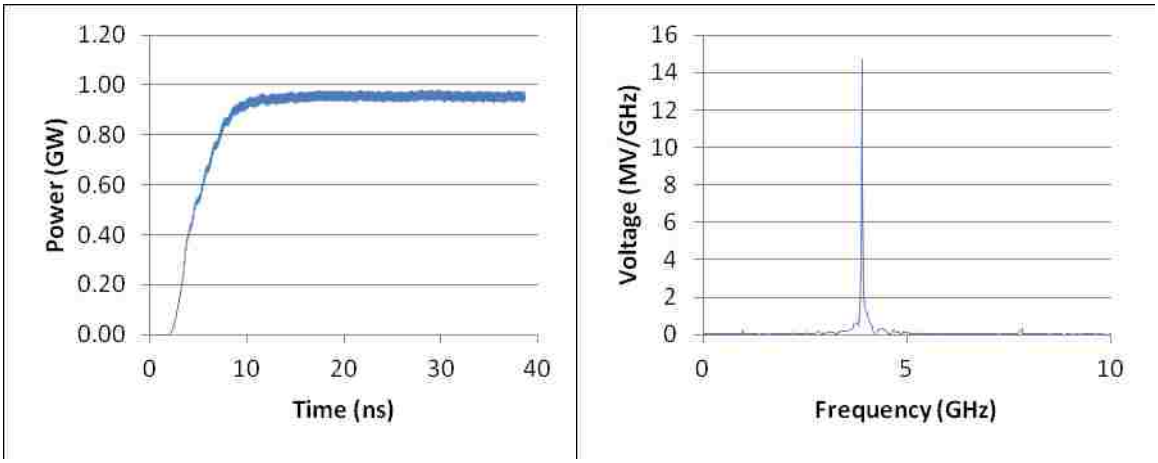

Figure 3.44. Output power (left), frequency spectrum of the RF signal (right) for magnetron with 2 recessed straps, the first with inner and outer radii of 27 mm and 28 mm, respectively, and the second with inner and outer radii of 29 mm and 30mm, respectively, at a magnetic field of 0.66 T and large cathode radius.

Figure 3.45 shows the middle cathode radius performance demonstrated a much larger variation depending on magnetic field values. Figure 3.46 shows the development of a significant π-mode factor that did not show in the large radius cathode runs.

Note in Fig. 3.47 the growth of a competing mode, possibly the 4/3 π-mode considering the four spokes shown, oscillating at 2.97 GHz as the magnetic field increases to 0.60 T leading to the dramatic drop in power output seen at that magnetic field value. For both 0.58 T and 0.62 T, the frequency spectrum more closely resembles that shown above in Fig. 3.46.

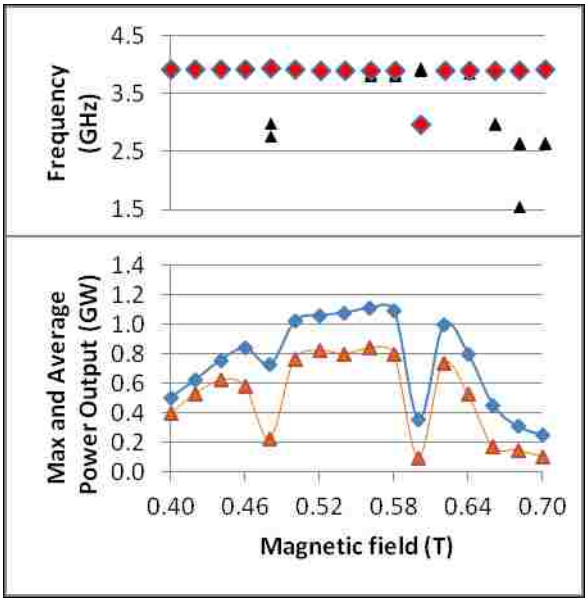

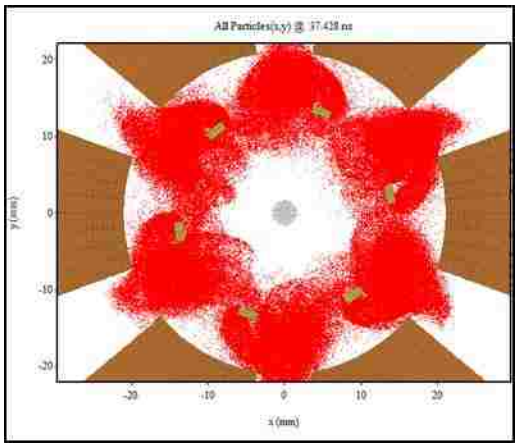

Figure 3.45. Power output and primary frequency as a function of magnetic field (left) and particle plot at saturation with a magnetic field of 0.56 T demonstrating 2π-mode operation (right) for magnetron with 2 recessed straps, the first with inner and outer radii of 27 mm and 28 mm, respectively, and the second with inner and outer radii of 29 mm and 30mm, respectively, and middle cathode radius.

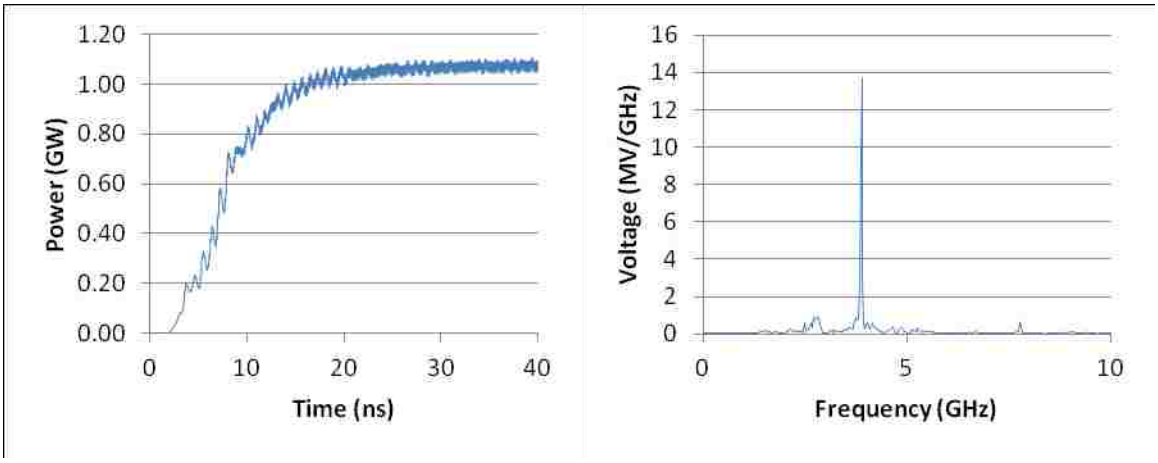

Figure 3.46. Output power (left), frequency spectrum of the RF signal (right) for magnetron with 2 recessed straps, the first with inner and outer radii of 27 mm and 28 mm, respectively, and the second with inner and outer radii of 29 mm and 30mm, respectively, at a magnetic field of 0.56 T and middle cathode radius.

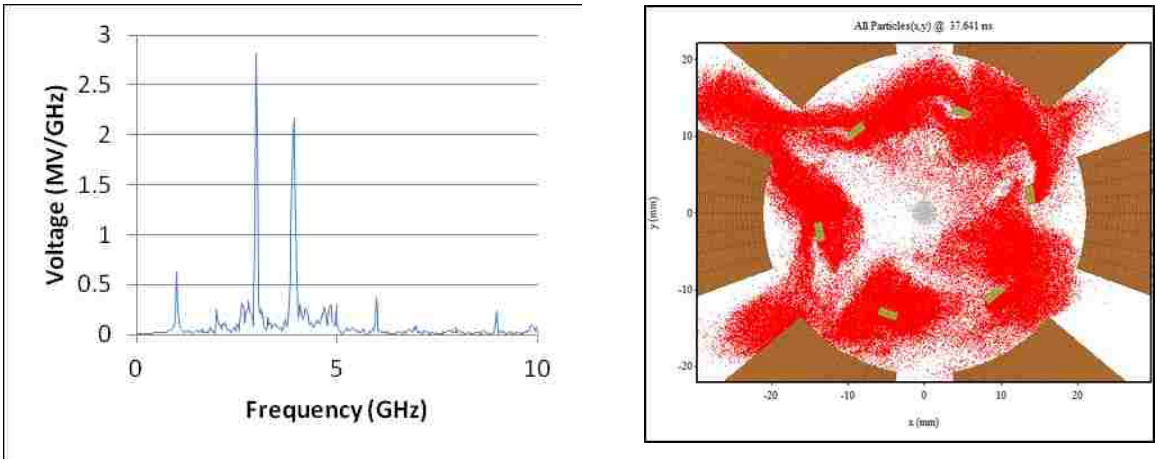

Figure 3.47. Frequency spectrum of the RF signal for magnetron with 2 recessed straps, the first with inner and outer radii of 27 mm and 28 mm, respectively, and the second with inner and outer radii of 29 mm and 30mm, respectively, and middle cathode radius, at a magnetic field of 0.60 T (left) and particle plot at saturation showing significant mode competition (right).

The smallest cathode radius produced 42% higher output power compared to the endcap version while radiating at 2.80 GHz but continued to operate at 2% lower efficiency as noted in the large and middle cathode radius configurations. The general output trend as shown in Fig. 3.48 indicates higher output performance at all frequencies compared to the endcap version. Figure 3.49 shows the dominance of the π-mode oscillations but also the significant interference from the 2π-mode at 3.90 GHz. This interference pattern was also seen at 0.46 T, though it was not quite as pronounced.

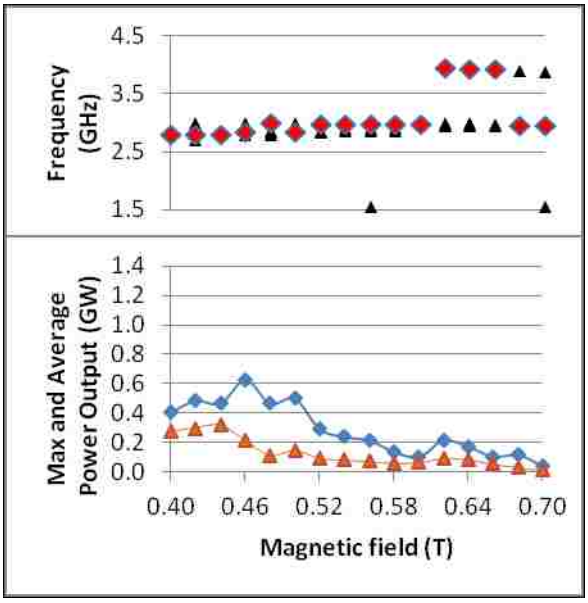

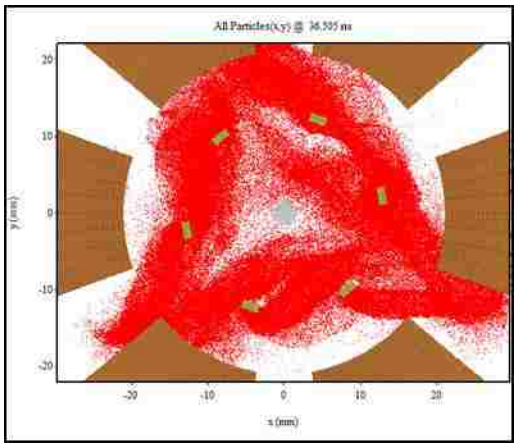

Figure 3.48. Power output and primary frequency as a function of magnetic field (left) and particle plot at saturation with a magnetic field of 0.42 T demonstrating contaminated π-mode operation (right) for magnetron with 2 recessed straps, the first with inner and outer radii of 27 mm and 28 mm, respectively, and the second with inner and outer radii of 29 mm and 30mm, respectively, and small cathode radius.

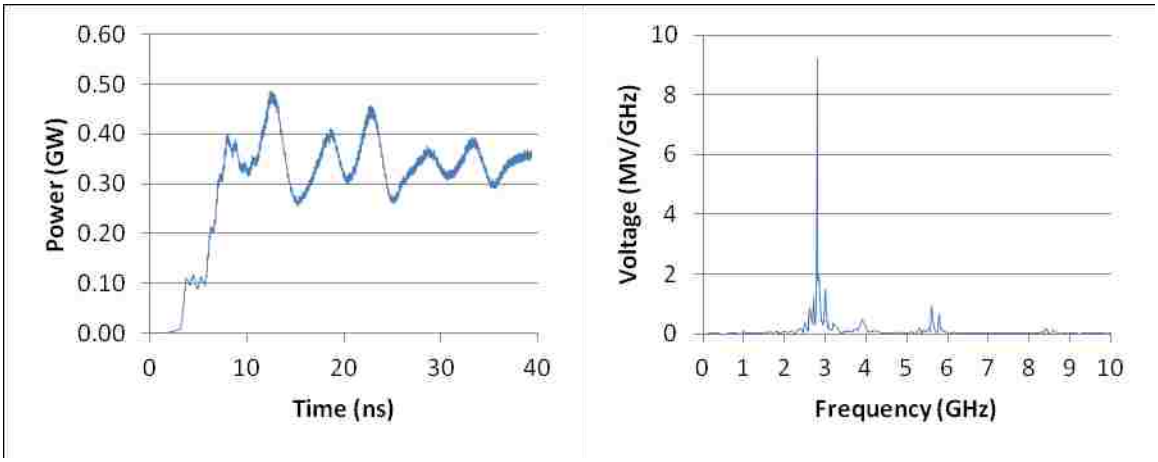

Figure 3.49. Output power (left), frequency spectrum of the RF signal (right) for magnetron with 2 recessed straps, the first with inner and outer radii of 27 mm and 28 mm, respectively, and the second with inner and outer radii of 29 mm and 30mm, respectively, at a magnetic field of 0.42 T and small cathode radius.

3.3.7 Magnetron with Single Strap Tied to All Vanes

The single strap tied to all 6 vanes showed marked performance improvements over the single strap tied to only three vanes with the standard radius cathode, although performance depended heavily on the magnetic field value, as shown in Fig. 3.50. Figure 3.51 shows generally similar frequency content to the double strap case as shown in Fig. 3.31 above except the nearest frequencies to the peak are suppressed slightly.

The middle cathode did not perform at all as expected. As shown in Fig. 3.52, the single strap tied to all 6 vanes performed extremely poorly across most of the magnetic field values evaluated, yielding only 20% of the endcap version's output power at 0.56 T. Figure 3.53 shows the inconsistent power output caused by multiple resonant frequencies.

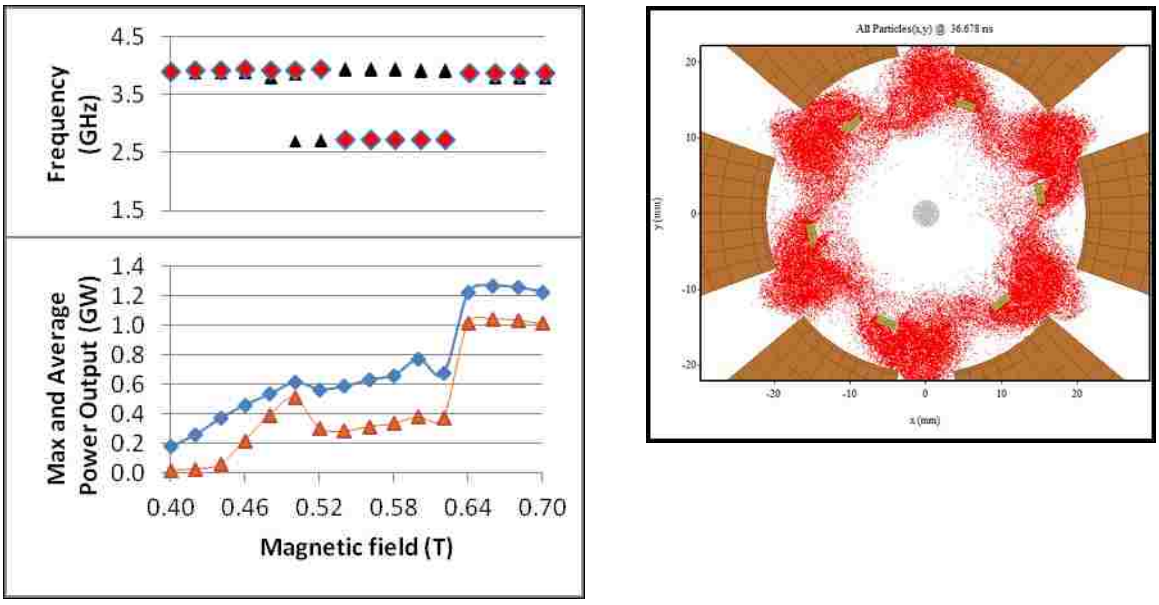

Figure 3.50. Power output and primary frequency as a function of magnetic field (left) and particle plot at saturation with a magnetic field of 0.66 T demonstrating 2π-mode operation (right) for magnetron with a single strap tied to all 6 vanes and large cathode radius.

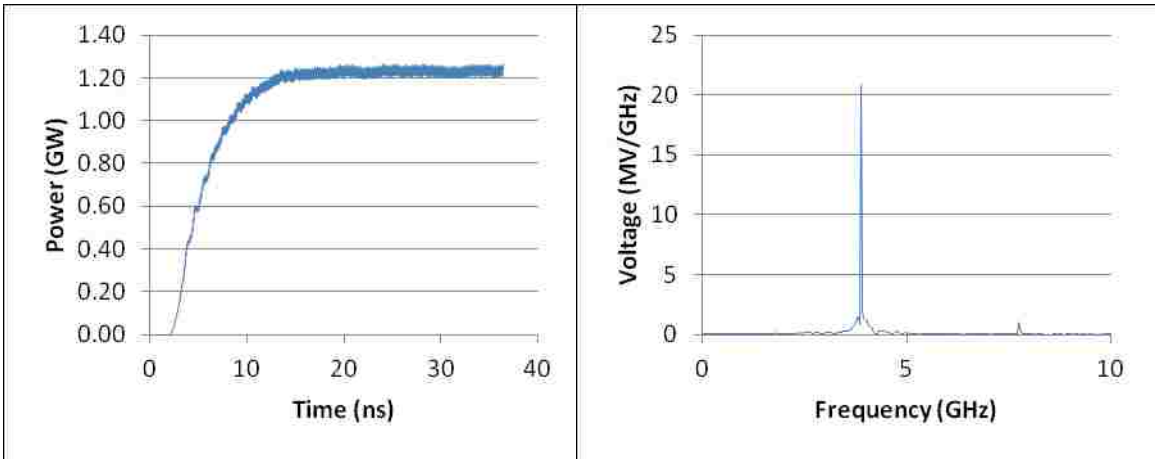

Figure 3.51. Output power (left), frequency spectrum of the RF signal (right) for magnetron with a single strap tied to all 6 vanes with inner and outer radii of 23 mm and 27 mm, respectively, at a magnetic field of 0.66 T and large cathode radius.

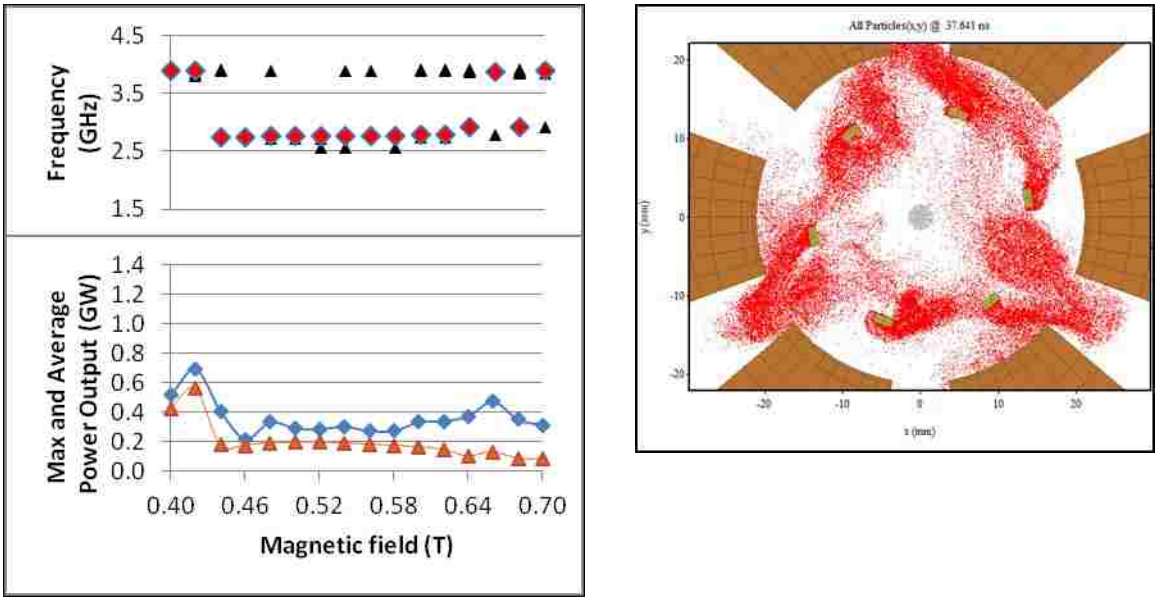

Figure 3.52. Power output and primary frequency as a function of magnetic field (left) and particle plot at saturation with a magnetic field of 0.56 T demonstrating contaminated π-mode operation (right) for magnetron with a single strap tied to all 6 vanes and middle cathode radius.

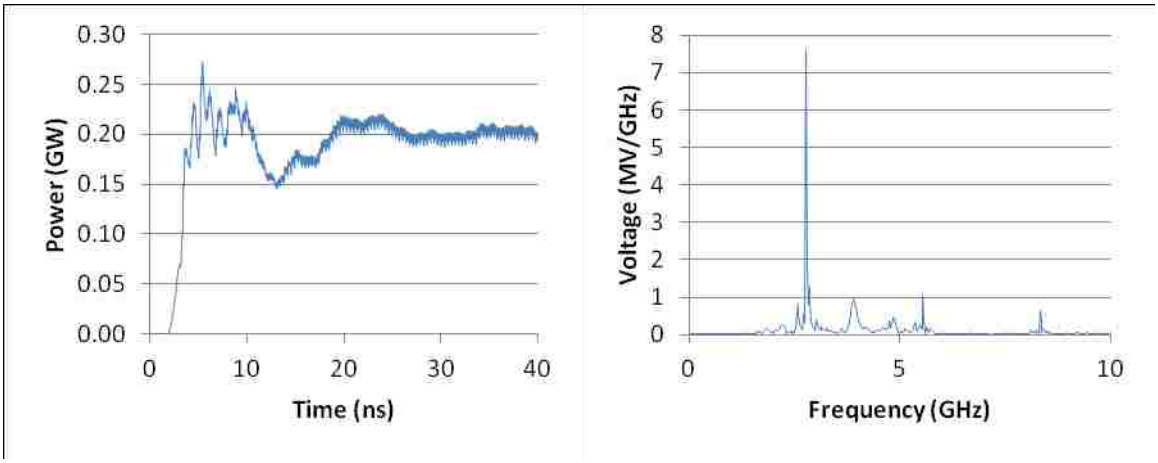

Figure 3.53. Output power (left), frequency spectrum of the RF signal (right) for magnetron with a single strap tied to all 6 vanes with inner and outer radii of 23 mm and 27 mm, respectively, at a magnetic field of 0.56 T and middle cathode radius.

Figure 3.54 shows the performance of the single strap tied to all 6 vanes with the medium cathode radius at 0.42 T; note the ringing in the power output profile and the peak of a secondary frequency, probably the π-mode, at 2.725 GHz.

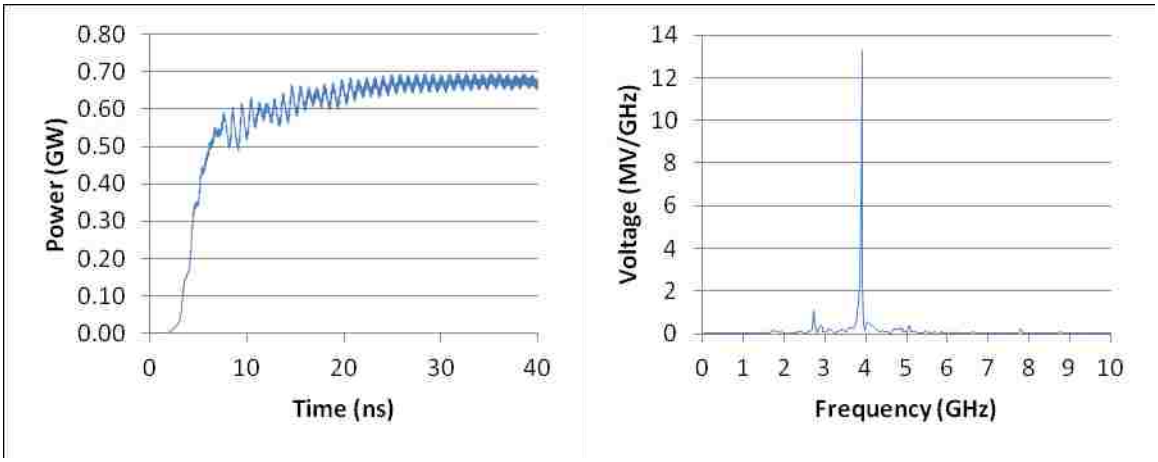

Figure 3.54. Output power (left), frequency spectrum of the RF signal (right) for magnetron with a single strap tied to all 6 vanes with inner and outer radii of 23 mm and 27 mm, respectively, at a magnetic field of 0.42 T and middle cathode radius.

The small cathode similarly performed poorly, only effectively oscillating at three magnetic field values as shown in Fig. 3.55 and then predominantly in the π-mode. It is worth noting, however, that the primary frequency of 2.775 GHz was much lower than

the 3.325 GHz observed with the endcap configuration which correlates to an almost 20% increase in wavelength. Figure 3.56 shows the dominant π-mode in the frequency output when operated at 0.42 T where this version produced less than 50% the power output of the endcap version. Power output improved to an 11% increase in average output power at 0.56 T, though still with predominantly π-mode operation and a 2% decrease in efficiency.

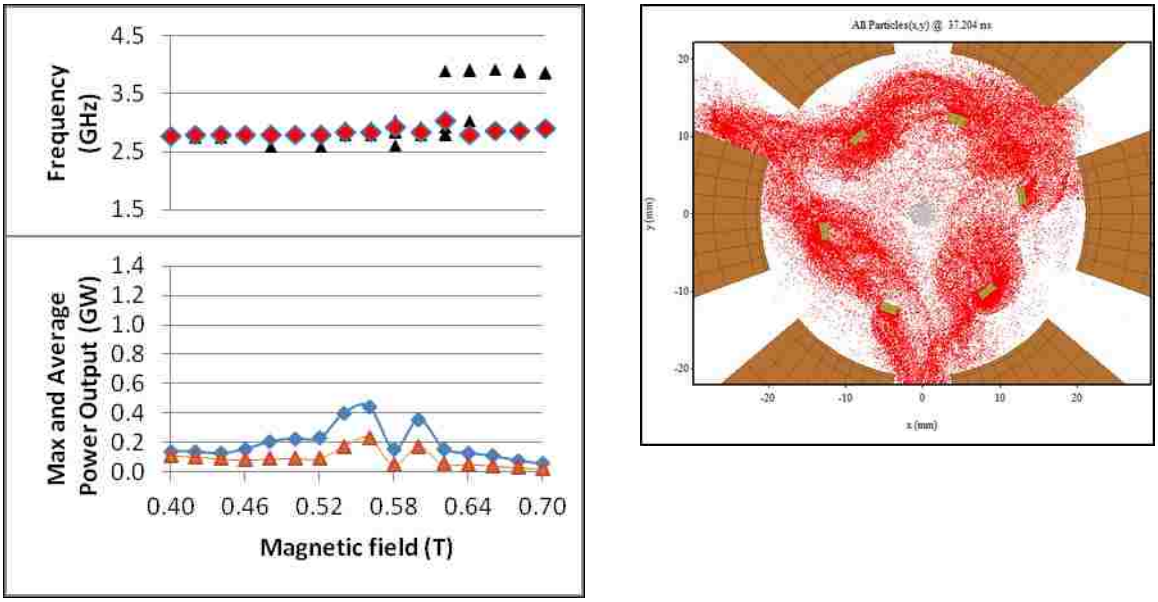

Figure 3.55. Power output and primary frequency as a function of magnetic field (left) and particle plot at saturation with a magnetic field of 0.42 T demonstrating contaminated π-mode operation (right) for magnetron with a single strap tied to all 6 vanes and small cathode radius.

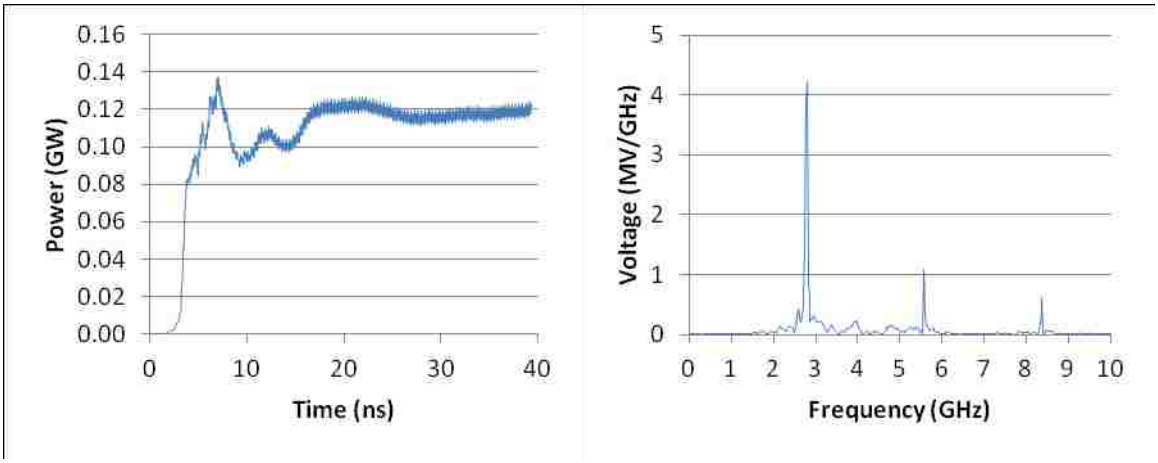

Figure 3.56. Output power (left), frequency spectrum of the RF signal (right) for magnetron with a single strap tied to all 6 vanes with inner and outer radii of 23 mm and 27 mm, respectively, at a magnetic field of 0.42 T and small cathode radius.

3.4 Summary of Results

For nearly all geometries studied, the largest cathode radius settled quickly into a 2π-mode oscillation. Even the non-endcap configuration produced comparable power output to the endcap version, albeit with significantly greater mode competition, though this is believed to be primarily a result of the transparent cathode; Palevsky and Bekefi reported an approximately 30% increase in power when using the anode endcaps with a traditional solid cathode [18].

The middle cathode radius began to show some differences between the geometries considered. While the endcap version matched very closely to the large cathode radius, the double strap and wide strap showed increased mode competition effects. The non-endcap geometry seemed to be approaching π-mode operation but displayed significant mode competition. This cathode radius showed the most variability in preferred mode between the geometries considered.

With the smallest cathode radius, the endcap configuration settled into a fairly stable π-mode operation at 0.42 T. The other configurations had more mode competition even with magnetic field values where they operated more efficiently or produced higher power than the endcap version. Optimum performance for all geometries at this cathode radius occurred in regions where π-mode operation was dominant.

Table 3.1 shows a brief summary of the output results for each strap configuration using the large cathode radius to provide comparison numbers between the endcap and other versions. The highest output power for each version is included along with the average output power and efficiency. Note that for the single strap and double strap configurations the peak performance occurred at the same magnetic field as the peak for the endcap version. Table 3.2 and Table 3.3 list similar information for the middle and small cathode radii, respectively.

Table 3.1. Summary of simulation results for large cathode radius showing magnetic field in Tesla, maximum output power in GW, average output in GW, and the efficiency of operation for 0.66 T and, if not at 0.66 T, the highest performing magnetic field for each strap configuration.

	B-field (T)	Max Output Power (GW)	Average Output Power (GW)	Primary Frequency (GHz)	Efficiency
endcap	0.66	1.083465	0.905326	4.200	16.14%
non-endcap	0.66	0.956039	0.731689	3.750	12.87%
	0.70	1.011863	0.818966	3.750	14.30%
single strap	0.66	1.142214	0.958879	3.950	16.20%
double strap	0.66	1.210111	1.002794	3.875	17.20%
wide strap	0.66	1.125185	0.945395	3.975	16.35%
	0.68	1.131928	0.942803	3.975	17.25%
recessed straps	0.66	0.980572	0.832026	3.900	13.92%
	0.58	0.996912	0.790730	3.950	13.45%
single strap tied to all 6 vanes	0.66	1.268065	1.047140	3.875	17.75%

Table 3.2. Summary of simulation results for middle cathode radius showing magnetic field in Tesla, maximum output power in GW, average output in GW, and the efficiency of operation for 0.56 T and, if not at 0.56 T, the highest performing magnetic field for each strap configuration.

	B-field (T)	Max Output Power (GW)	Average Output Power (GW)	Primary Frequency (GHz)	Efficiency
endcap	0.56	1.135887	0.915903	4.175	22.95%
non-endcap	0.56	0.201355	0.124392	2.525	4.05%
	0.40	0.464549	0.392340	3.775	7.18%
single strap	0.56	1.131091	0. 879990	3.925	21.74%
	0.54	1.135355	0.906923	3.950	20.71%
double strap	0.56	1.213684	0.950889	3.875	24.27%
wide strap	0.56	0.355752	0.188903	3.000	8.03%
	0.60	1.003088	0.804354	3.975	25.28%
recessed straps	0.56	1.108842	0.842203	3.900	20.34%
single strap tied to all 6 vanes	0.56	0.273325	0.182909	2.775	5.56%
	0.42	0.695145	0.562292	3.900	11.99%

Table 3.3. Summary of simulation results for small cathode radius showing magnetic field in Tesla, maximum output power in GW, average output in GW, and the efficiency of operation for 0.42 T and, if not at 0.42 T, the highest performing magnetic field for each strap configuration.

	B-field (T)	Max Output Power (GW)	Average Output Power (GW)	Primary Frequency (GHz)	Efficiency
endcap	0.42	0.313137	0.208405	3.325	13.91%
non-endcap	0.42	0.110254	0.082269	2.525	2.31%
	0.54	0.238534	0.142417	2.600	7.80%
single strap	0.42	0.151361	0.065510	3.000	3.56%
	0.58	0.439704	0.267318	3.125	18.85%
double strap	0.42	0.163374	0.081991	2.950	3.87%
	0.56	0.415494	0.254170	3.050	16.34%
wide strap	0.42	0.132474	0.106493	3.000	3.11%
	0.54	0.406297	0.166080	3.125	15.49%
recessed straps	0.42	0.486585	0.297739	2.800	11.18%
	0.46	0.630620	0.217286	2.850	16.52%
single strap tied to all 6 vanes	0.42	0.137448	0.103338	2.775	3.01%
	0.56	0.442367	0.232428	2.850	11.84%

CHAPTER 4 CONCLUSIONS

In this chapter, specific simulation cases addressing comparisons between this work and the standard issues considered for non-relativistic magnetrons are discussed. General conclusions are described and recommendations are made for further study.

4.1 Additional Considerations

This section discusses the effect of moving the spacers for the rings in the θ-direction, thickening the straps in the z-direction, and introducing a break in the straps.

4.1.1 Spacer Locations

The spacers for all strap configurations were centered in the θ-direction on the respective vanes. This choice was initially made as a convenience but was later examined for possible effect on the performance of the strapping solutions employed. To examine potential effects from this design choice, a short sequence of simulations was performed using the modified single strap configuration with each strap tied to all 6 vanes using the large cathode radius at 0.66 T. The spacers were moved π/18 radians counter-clockwise and clockwise for the different simulations.

As shown in Fig. 4.1, moving the spacers counter-clockwise, or in the positive θ-direction, increased the π-mode component slightly and resulted in a 13% decrease in output power. However, moving the spacers clockwise, in the negative θ-direction, caused the π-mode to become dominant but reduced the output power by 63%.

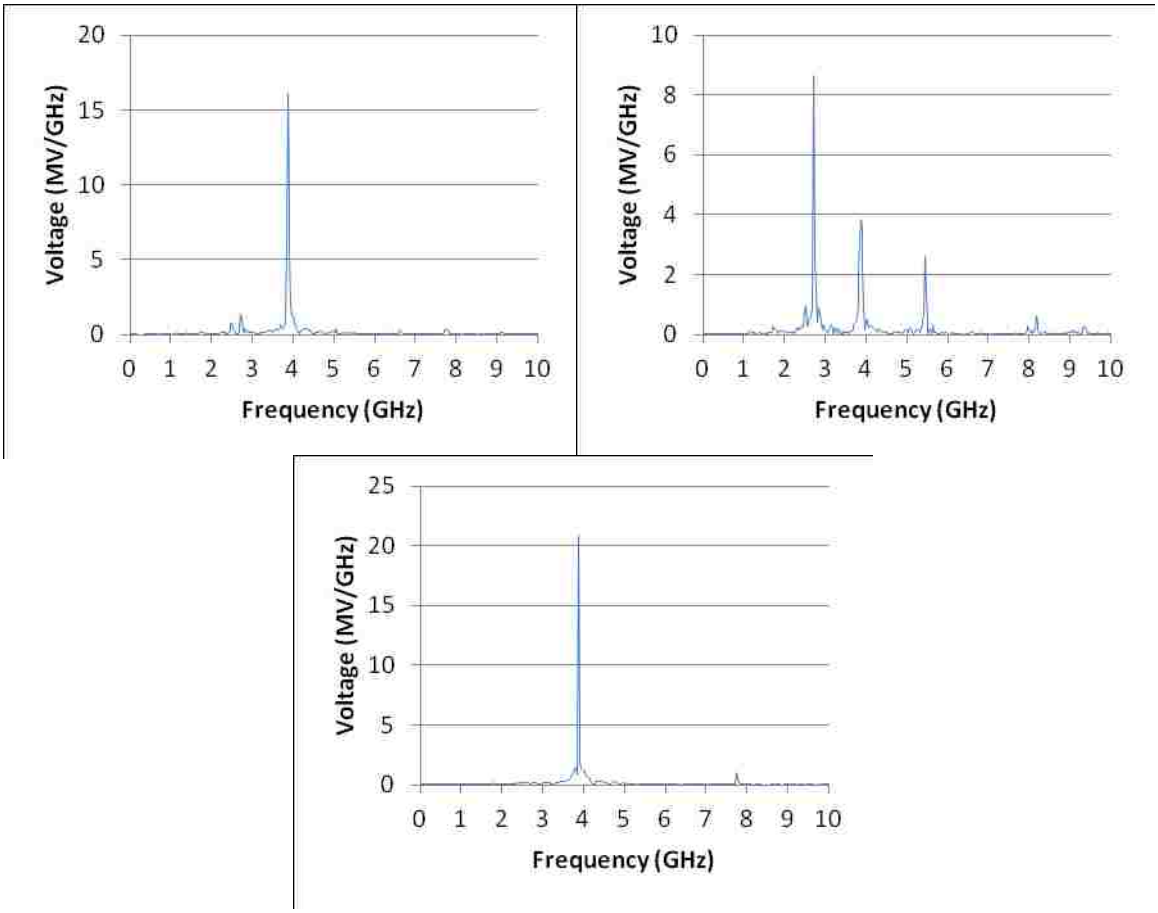

Figure 4.1. FFT showing effect of moving spacers π/18 radians counterclockwise (top left) and clockwise (top right) for the single strap tied to all 6 vanes with large radius cathode compared to the original position (bottom).

4.1.2 Thickness of Straps

The initial studies all used straps of the same thickness, 1.8 mm, which was 1/40th the length of the vane in the axial direction. This value was selected more as a matter of convenience than for any mathematical or theoretical consideration. After the bulk of the study was completed, a set of simulations looked at the double-strap configuration with a magnetic field of 0.64 T with the small cathode radius to vary the thickness in the z-direction of the strapping. This configuration was chosen because the double strap approach generally performed well but displayed strong mode competition

at this magnetic field value. Three simulations were performed using straps doubled, quadrupled, and halved compared to the thickness used throughout the study; the frequency FFTs are shown in Fig. 4.2.

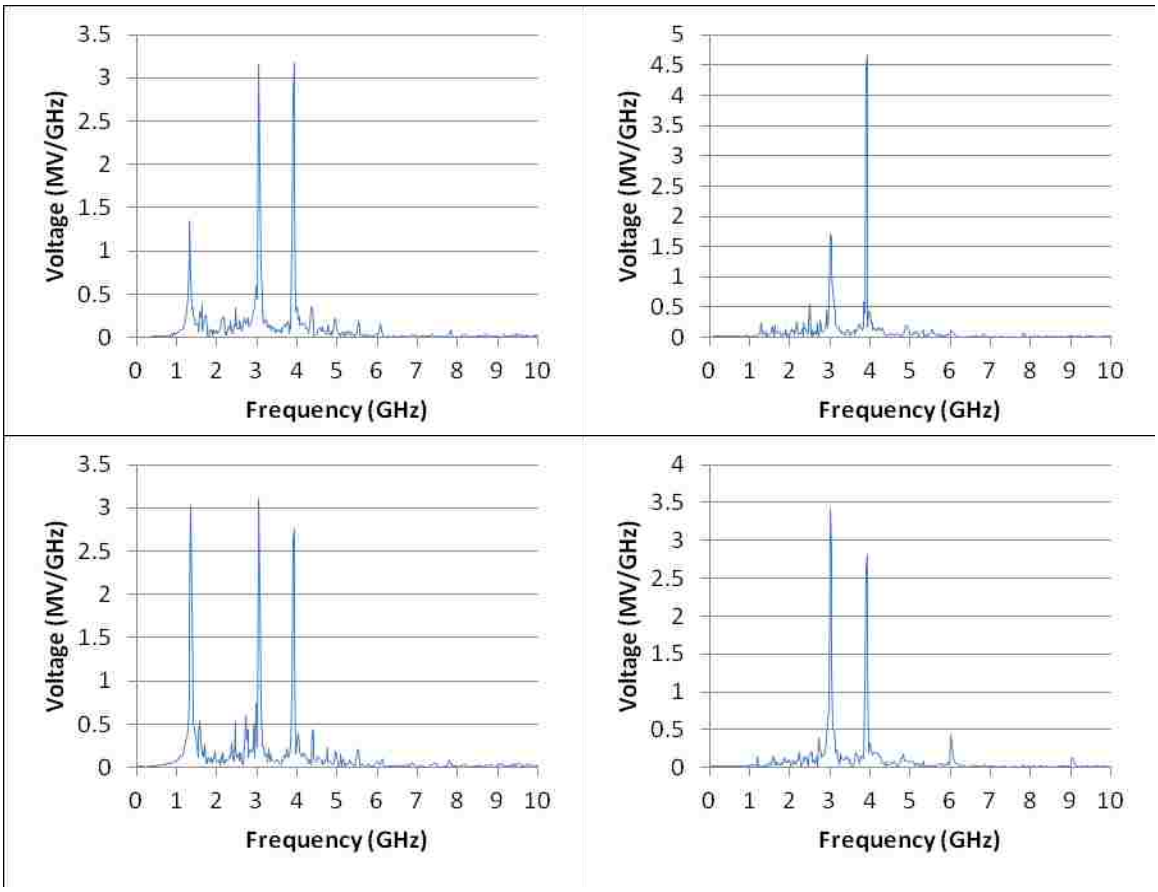

Figure 4.2. Frequency spectrum of double ring configuration with small radius cathode at 0.64 T comparing strap thickness; base strap thickness (top left) shows significant mode competition that is reduced by the doubled strap thickness (top right). The halved thickness (bottom left) suffered worse mode competition than the base thickness while the quadrupled thickness (bottom right) more closely resembled the double thickness plot.

The doubled thickness considerably reduced the intensity of the π-mode as well as the modes occurring at lower frequencies. However, it radiated 32% less output power than the original thickness. The quadrupled thickness also reduced mode competition significantly but radiated 43% less power. The half thickness configuration showed

increased mode competition, particularly at 1.35 GHz, yet produced 27% more output power than the original strap thickness.

4.1.3 Strap Breaks

One factor discussed by Collins [7] is the introduction of an asymmetry to the strapping system by including a break in one strap either up- or down-stream from the anode block. To evaluate this effect, four simulations were performed, again using the double strap configuration at 0.64 T as the starting point. A break was introduced over the vane in a different strap for each simulation; only a single break was involved in each. This break was located at the same angular location as the supporting spacer for the other strap; see Fig. 4.3 for reference.

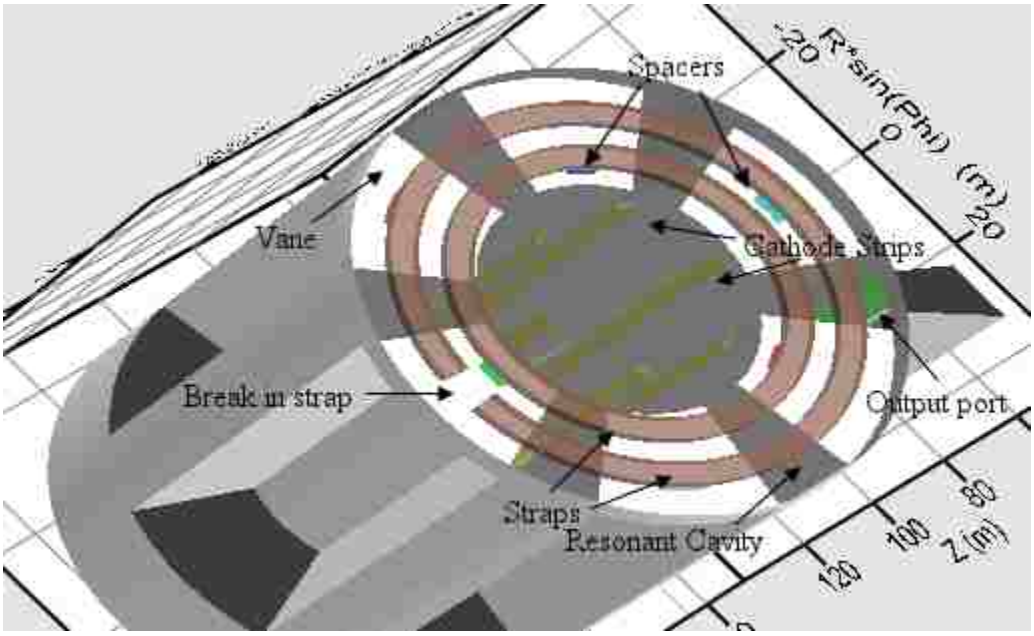

Figure 4.3. Cut-away view of double-strap configuration indicating a break in the downstream strap.

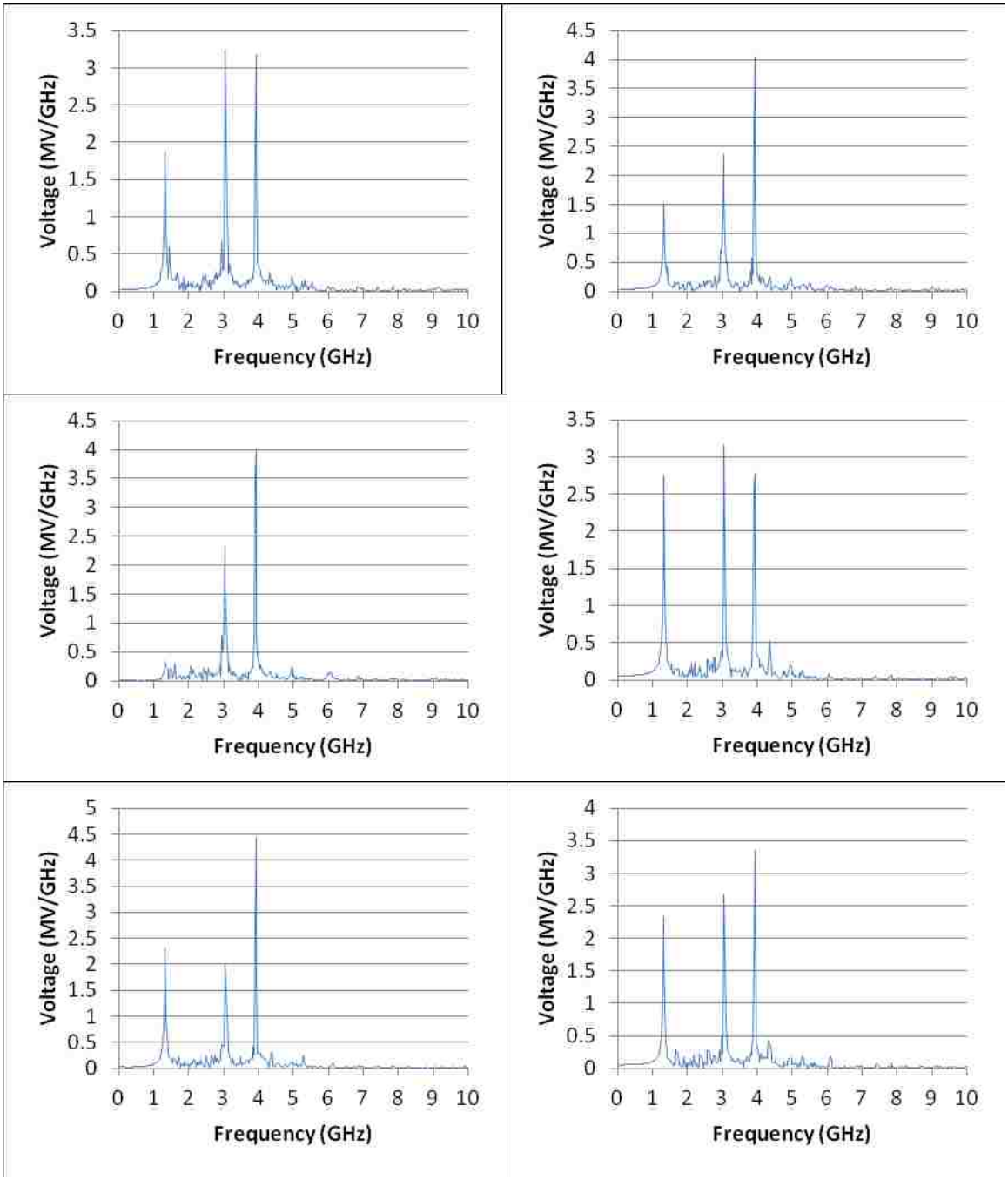

Figure 4.4. FFTs showing the effect of incorporating breaks in the straps for the double strap configuration with small radius cathode at 0.64 T. Breaks are located on the downstream inner strap (top left), upstream inner strap (top right), downstream outer strap (middle left), upstream outer strap (middle right), both downstream straps (lower left) and both upstream straps (lower right).

Figure 4.4 shows the frequency results from the strap break studies. In all 6 cases the overall performance for both power output and efficiency was between 1-5% lower

than the basic double strap performance. However, the frequency shifted slightly up to 3.90 GHz as was seen earlier when increasing the thickness of the straps. The benefit of the asymmetry introduced by the strap break does not appear to carry over to a magnetron operating in the 2π-mode; perhaps not surprising considering the 6-fold symmetry in fields and particle motion compared to the 3-fold symmetry of the π-mode.

4.2 Recommendations for Further Study

In general, strapping appears to offer several advantages for use in the A6 magnetron. For conditions where the A6 performs well, replacing the anode endcaps with either the double strap or the single strap tied to each vane produced 10-15% greater output power with an increase in operating efficiency as well. For conditions where the A6 does not perform well, such as when employing a small cathode, the double strap reduced the mode competition seen in many cases.

It bears repeating that this study, being simulation only, does not address the issue of arcing that has been raised as a primary argument against the use of straps in a relativistic magnetron. An experimental study to determine the likelihood and severity of arcing could address this question readily by isolating the conditions under which arcing is most likely. This information could then be combined with additional simulations to determine the optimum strap dimensions for use in a given situation.

An in-depth analytical description of the strap and its effect on the magnetron's performance would significantly aid the optimization effort. Repeating parts of this study using a solid cathode, which generally displays more mode competition than the transparent cathode, would also provide insight into the behavior and effects of the strapping. Shortening the anode block so that it approaches one-third the wavelength of

the dominant frequency, as is more customary with the conventional strapped magnetron, should increase the capacitive effect of the straps and enhance their performance as well. In addition, using a magnetron with more cavities, which typically results in increased mode competition, may further validate the utility of strapping in relativistic magnetrons.

REFERENCES

[1] A. Andreev and K. Hendricks, "First multi-cavity magnetrons were built in NII-9, Leningrad, during the spring of 1937 PIC simulations of the first 4-cavity S-band CW magnetron," *2010 International Conference on the Origins and Evolution of the Cavity Magnetron (CAVMAG),* pp. 71-75, 2010.

[2] J. Goerth, "Early magnetron development especially in Germany," *2010 International Conference on the Origins and Evolution of the Cavity Magnetron (CAVMAG),* pp. 17-22, 2010.

[3] J. Benford, "History and future of the relativistic magnetron," *2010 International Conference on the Origins and Evolution of the Cavity Magnetron (CAVMAG),* pp. 40-45, 2010.

[4] A. Das and S. K. Das, Microwave Engineering, 2nd ed., Delhi: Tata McGraw Hill Publishing Company, 2009, pp. 377-384.

[5] R. Barker, N. Luhmann, J. Booske and G. Nusinovich, Modern Microwave and Millimeter-Wave Power Electronics, 1st ed., Piscataway, NJ: Wiley-IEEE Press, 2005, pp. 291-296.

[6] A. S. Gilmour, Microwave Tubes, 1st ed., Morwood, MA: Artech House, 1986.

[7] G. B. Collins, Microwave Magnetrons, 1st ed., G. Collins, Ed., New York: McGraw Hill, 1948.

[8] J. Benford, J. A. Swegle and E. Schamiloglu, High Power Microwaves, 2nd ed., Boca Raton: Taylor & Francis Group, 2007.

[9] R. Lemke, T. Genoni and T. Spencer, "Effects that limit efficiency in relativistic

magnetrons," *IEEE Transactions on Plasma Science,* vol. 28, no. 3, pp. 887-897, 2000.

[10] M. Brady and M. Edwards, "Developments in marine radar magnetrons," *2010 International Conference on the Origins and Evolution of the Cavity Magnetron (CAVMAG),* pp. 58-63, 2010.

[11] V. Neculaes, M. Jones, R. Gilgenbach, Y. Lau, J. Luginsland, B. Hoff, W. White, N. Jordan, P. Pengvanich, Y. Hidaka and H. Bosman, "Magnetic priming effects on noise, startup, and mode competition in magnetrons," *IEEE Transactions on Plasma Science,* vol. 33, no. 1, pp. 94-102, 2005.

[12] B. Hoff, M. Franzi, R. Gilgenbach and Y. Lau, "Three-Dimensional Simulations of Magnetic Priming of a Relativistic Magnetron," *IEEE Transactions on Plasma Science,* vol. 38, no. 6, pp. 1292-1301, 2010.

[13] D. Kaup, "Theoretical Modeling of an A6 Relativistic Magnetron," *Physics of Plasmas,* vol. 11, no. 6, pp. 3151-3164, 2004.

[14] A. Andreev, K. Hendricks, M. Fuks and E. Schamiloglu, "Analytical calculation of anode current in relativistic magnetron," *Proceedings of IEEE Pulsed Power Conference, 2009,* pp. 502-506, 2009.

[15] Y. Alfadhl, D. Li and X. Chen, "Advanced computer modelling of magnetrons," *2010 International Conference on the Origins and Evolution of the Cavity Magnetron (CAVMAG),* pp. 67-70, 2010.

[16] "ATK Missions Systems," ATK-MRC, [Online]. Available: http://www.mrcwdc.com/magic/index.html. [Accessed 14 January 2012].

[17] H. L. Bosman, M. I. Fuks, S. Prasad and E. Schamiloglu, "Improvement of the Output Characteristics of Magnetrons Using the Transparent Cathode," *IEEE Transactions on Plasma Science*, vol. 34, no. 3, pp. 606-619, June 2006.

[18] A. Palevsky and G. Bekefi, "Microwave emission from pulsed, relativistic e-beam diodes. II. The multiresonator magnetron," *Physics of Fluids*, vol. 22, no. 5, pp. 986-996, 1979.

[19] T. Treado, W. Doggett, G. Thomas, R. I. Smith, J. Jackson-Ford and D. Jenkins, "Operating modes of relativistic rising-sun and A6 magnetrons," *IEEE Transactions on Plasma Science*, vol. 16, no. 2, pp. 237-248, 1988.

[20] A. Palevsky, "Generation of intense microwave radiation by the relativistic e-beam magnetron (experiment and numerical simulation)," Massachusetts Institute of Technology, Boston, 1980.

[21] M. Fuks and E. Schamiloglu, "Rapid Start of Oscillations in a Magnetron with a "Transparent" Cathode," *Physical Review Letters*, vol. 95, no. 20, pp. 205101-1-205101-4, 2005.

[22] S. Prasad, M. Roybal, C. Buchenauer, K. Prestwich, M. Fuks and E. Schamiloglu, "Experimental verification of the advantages of the transparent cathode in a short-pulse magnetron," *Pulsed Power Conference, 2009*, pp. 81-85, 2009.

[23] Y. Saveliev, W. Sibbett, S. Spark, B. Kerr, M. Harbour and S. Douglas, "Comparative study of a relativistic magnetron performance with various cathodes," *Digest of Technical Papers, 12th IEEE International Pulsed Power Conference*, vol. 1, pp. 198-201, 1999.

[24] L. Ma, "3D Computer Modeling of Magnetrons," University of London Department of Electronic Engineering, London, 2004.

[25] P. Pengvanich, "Theory of Injection Locking and Rapid Start-Up of Magnetrons, and Effects of Manufacturing Errors in Terahertz Traveling Wave Tubes," University of Michigan Department of Nuclear Engineering and Radiological Sciences, Ann Arbor, 2007.

[26] M. Lopez, R. Gilgenbach, D. Jordan, S. Anderson, M. Johnston, M. Keyser, H. Miyake, C. Peters, M. Jones, V. Bogdan Neculaes, Y. Y. Lau, T. Spencer, J. Luginsland, M. Haworth, R. Lemke and D. Price, "Cathode effects on a relativistic magnetron driven by a microsecond e-beam accelerator," *IEEE Transactions on Plasma Science*, vol. 30, no. 3, pp. 947-955, 2002.